Raman spectroscopy as a tool to determine the thermal maturity of organic matter: Application to sedimentary, metamorphic and structural geology

Delano G. Henry[a,*], Ian Jarvis[a], Gavin Gillmore[a], Michael Stephenson[b]

[a] Department of Geography, Geology and the Environment, Kingston University London, Kingston upon Thames KT1 2EE, UK
[b] British Geological Survey, Keyworth, Nottingham NG12 5GG, UK

A B S T R A C T

Raman spectrometry is a rapid, non-destructive alternative to conventional tools employed to assess the thermal alteration of organic matter (OM). Raman may be used to determine vitrinite reflectance equivalent OM maturity values for petroleum exploration, to provide temperature data for metamorphic studies, and to determine the maximum temperatures reached in fault zones. To achieve the wider utilisation of Raman, the spectrum processing method, and the positions and nomenclature of Raman bands and parameters, all need to be standardized. We assess the most widely used Raman parameters as well as the best analytical practices that have been proposed. Raman band separation and G-band full-width at half-maximum are the best parameters to estimate the maturity for rocks following diagenesis–metagenesis. For metamorphic studies, the ratios of band areas after performing deconvolution are generally used. Further work is needed on the second-order region, as well as assessing the potential of using integrated areas on the whole spectrum, to increase the calibrated temperature range of Raman parameters. Applying Raman spectroscopy on faults has potential to be able to infer both temperature and deformation processes. We propose a unified terminology for OM Raman bands and parameters that should be adopted in the future. The popular method of fitting several functions to a spectrum is generally unnecessary, as Raman parameters determined from an un-deconvoluted spectrum can track the maturity of OM. To progress the Raman application as a geothermometer a standardized approach must be developed and tested by means of an interlaboratory calibration exercise using reference materials.

1. Introduction

Raman spectroscopy is increasingly being used to determine the thermal alteration (maturity) of organic matter (OM). The novelty of Raman spectroscopy is that it is a rapid and non-destructive technique that can be used to complement other methods or it can be employed independently, and it offers a means to screen samples before more expensive and destructive analysis (Sauerer et al., 2017; Schmidt et al., 2017; Henry et al., 2018, 2019; Khatibi et al., 2018b; Schito and Corrado, 2018; Wilkins et al., 2018). Raman spectroscopy is now part of a wide selection of tools that can be used to track the thermal maturity of OM. These include: vitrinite reflectance (VR$_o$); bitumen reflectance; graptolite reflectance; chitinozoan reflectance; spore colouration index; OM fluorescence; organic geochemistry, including Rock-Eval™ pyrolysis and biomarker analysis (Hartkopf-Fröder et al., 2015). Having a selection of methods to determine OM maturity allows geoscientists to optimize their analysis based on the quantity, composition and age of the sample, maturity grade, operator expertise, equipment availability, and time and money constraints.

Tunistra and Koenig (1970) published the first paper showing two distinct Raman bands in graphite: the disordered (D) and graphite (G) bands. Beny-Bassez and Rouzaud (1985) highlighted the first use of Raman spectroscopy to determine the coalification and graphitization

stages of OM by studying samples that had been artificially heated; they were also the first authors to construct an empirical relationship with VR$_o$. Pasteris and Wopenka (1991) then applied Raman spectroscopy in a study of naturally metamorphosed carbonaceous metapelites in order to assess the metamorphic grade by conducting visual comparisons. Wopenka and Pasteris (1993) later demonstrated that the area ratio of the D and G bands are effective in determining the metamorphic grade of metamorphic rocks. Following this, Spötl et al. (1998) used natural samples to demonstrate that Raman spectroscopy may be used to determine equivalent VR$_o$ values for a wide maturity range (0.38–6.10% VR$_o$). Beyssac et al. (2002) derived the first temperature dependent empirical equation, in order to quantitively determine the peak temperature between 330 and 650 °C during metamorphism. This was a turning point, and the study encouraged the wider use of Raman spectroscopy as a geothermometer for geological samples, with an exponential increase in papers being published over the last 25 years (Fig. 1).

Raman spectroscopy has been used in three main applications as a geothermometer, to determine: (1) source rock maturity for hydrocarbon exploration (Liu et al., 2013; Sauerer et al., 2017; Schito et al., 2017, 2019; Schito and Corrado, 2018; Wang et al., 2018; Wilkins et al., 2018; Henry et al., 2019; Hou et al., 2019; Khatibi et al., 2019; Lupoi et al., 2019; Mi et al., 2019); (2) the maximum temperature reached
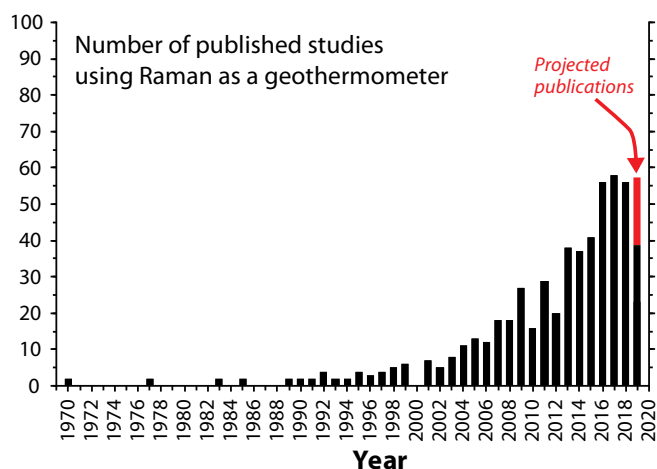
Fig. 1. Bar chart showing the exponential increase in studies that have used Raman spectroscopy as a geothermometer. The data were acquired from the Web of Science bibliography database and is by no means an exhaustive data set. Projected publications for 2019 is based on the number papers that were published during the same period for 2018.

during regional and contact metamorphism (Wopenka and Pasteris, 1993; Beyssac et al., 2002; Jehlička et al., 2003; Rahl et al., 2005; Aoya et al., 2010; Lahfid et al., 2010; Endo et al., 2012; Mathew et al., 2013; Kouketsu et al., 2014, 2019; Chen et al., 2017; Muirhead et al., 2017a, 2017b; Beyssac et al., 2019; Fomina et al., 2019; ; Yu et al., 2019; Zhang and Santosh, 2019); (3) the maximum temperature reached during frictional heating along fault planes after an earthquake (Furuichi et al., 2015; Kaneki et al., 2016; Liu et al., 2016; Kouketsu et al., 2017; Kuo et al., 2017, 2018; Kaneki and Hirono, 2018, 2019; Mukoyoshi et al., 2018). Studies have had various degrees of success, and due to widely varying methodologies, comparison of the results remains difficult. Here, we review the most commonly used and suitable Raman parameters for each application, as well as assess the best practices that have been proposed, in an attempt to encourage a standardized approach. We will also provide recommendations for future progress.

2. Thermal maturation of organic matter

Determining the maturity of OM is essential to confirm the presence of a working petroleum system and to establish the time-temperature history of geological events. When OM is exposed to high temperatures, it undergoes an irreversible chemical and structural evolution (Tissot and Welte, 1984), which makes it an ideal component to determine the maximum temperature reached in a sedimentary or metamorphic rock. This is in contrast to mineral assemblages, where temperature records may be reset by subsequent dissolution and recrystallization. However, different types of organic matter in a sedimentary rock respond differently to increased temperatures. This needs to be taken into consideration, as it has been shown to impact the Raman spectrum (Guedes et al., 2005, 2010).

Tissot and Welte (1984) determined four different stages of thermal maturation during burial: diagenesis, catagenesis, metagenesis, and metamorphism. Diagenesis occurs as soon as deposition has taken place, and stops when temperatures reach 60–80 °C (0–0.5%VR$_o$; Tissot and Welte, 1984). Here microbial degradation and low-temperature reactions destroy proteins and carbohydrate biopolymers, and the remaining more resistant constituents polycondense to form geopolymers and subsequently kerogen. By-products of diagenesis include CO_2, H_2O, H_2S, SO_2, N_2 and biogenic CH_4. Catagenesis ranges from c. 60–150 °C (0.6–2.0%VR$_o$) and the kerogen is subject to thermal decomposition reactions that break up large kerogen molecules to smaller kerogen molecules (Tissot and Welte, 1984). During early catagenesis oil is

mostly produced (0.5–1.3%VR$_o$), followed by the production of wet gas (1.3–2.0%VR$_o$; Tissot and Welte, 1984). Catagenesis is also associated with increased ordering of the OM. Metagenesis occurs at temperatures c. 150–200 °C (2.0–4.0%VR$_o$) and produces primary dry gas directly from the remaining kerogen and secondary gas from the cracking of longer chained hydrocarbons (Tissot and Welte, 1984). At the end of this stage, heteroatoms and hydrogen have all been depleted by carbonisation, and the residual carbon becomes disordered graphite that will undergo progressive graphitization during metamorphism, eventually becoming a perfectly ordered graphite with increasing temperatures and pressures (Landis, 1971; Buseck and Beyssac, 2014).

Alternative mechanisms that can thermally mature OM include: the emplacement of igneous intrusions (contact metamorphism); and frictional heating along fault planes (Buseck and Beyssac, 2014). What differs here, is the way in which the OM is heated. For burial, as described above, the OM is typically heated due to the geothermal gradient and radiogenic heat production (Tissot and Welte, 1984; Allen and Allen, 2013). Diagenesis, catagenesis and metagenesis occur over long-time scales at relatively low temperatures (< 200 °C) and impact a whole basin; similarly, regional metamorphism occurs over long-time scales with wide ranging effects, but at significantly higher temperatures (200–1000 °C; Hoinkes et al., 2005). Contact metamorphism may generate similar temperatures to regional metamorphism (200–1000 °C) but takes place over shorter time scales (10^3–10^6 years) and only matures OM locally within the thermal aureole (Hoinkes et al., 2005). Maturation of organic matter due to frictional heating along fault zones is associated with rapid heating rates of tens to hundreds of °C s^{-1}, along with substantial shearing, deformation and pulverization of the OM (Nakamura et al., 2015; Kaneki et al., 2016). There is no remnant heat that 'cooks' the country rock, unlike igneous intrusions; however, movement may occur multiple times along the same fault, thereby generating multiple episodes of heating.

It is widely acknowledged that temperature and time are the most important factors in the maturation process of OM (Beyssac et al., 2002; Allen and Allen, 2013); however, it is also crucial to understand how different heating rates, pressures and shearing/deformation impact the Raman spectra of OM. In order to get the most out of Raman spectroscopy as a geothermometer we must assess: (1) which parameters are best suited for each application; (2) whether different thermal and pressure conditions can be determined from OM Raman parameters or the visual appearance of the spectrum; (3) the extent to which shearing and pulverization of OM may impact the Raman spectrum; (4) whether different calibration curves are needed for OM that has experienced different time-temperature-pressure histories. Some of these questions have been asked and answered in different ways in the literature and will be addressed in this review.

3. Organic matter Raman bands and nomenclature

The Raman spectrum of OM is composed of a first-order region (1000–1800 cm^{-1}) and a second-order region (2400–3500 cm^{-1}). The first-order region comprises two main peaks; the disordered (D) band (c. 1340–1360 cm^{-1}) and the graphite (G) band (c. 1580 cm^{-1}) (Fig. 2a). The G-band is related to the in-plane vibration of carbon atoms in graphene sheets with E_{2g2} symmetry (Tunistra and Koenig, 1970; Jehlička and Beny, 1999). In graphite, this is the only major band in the first-order region.

The D-band occurs at c. 1340–1360 cm^{-1} in disordered amorphous OM and is associated with structural defects and heteroatoms (Beny-Bassez and Rouzaud, 1985). It has been described as the breathing motion of the sp^2 atoms in an aromatic ring with a A_{1g} symmetry mode vibration (Tunistra and Koenig, 1970). In disordered OM, additional bands are identifiable as small bumps and asymmetric bands, however, the number, nomenclature and origin of these bands are often conflicting when deconvolution is performed (Beyssac et al., 2002; Li et al., 2006; Romero-Sarmiento et al., 2014; Ferralis et al., 2016; Schito et al.,
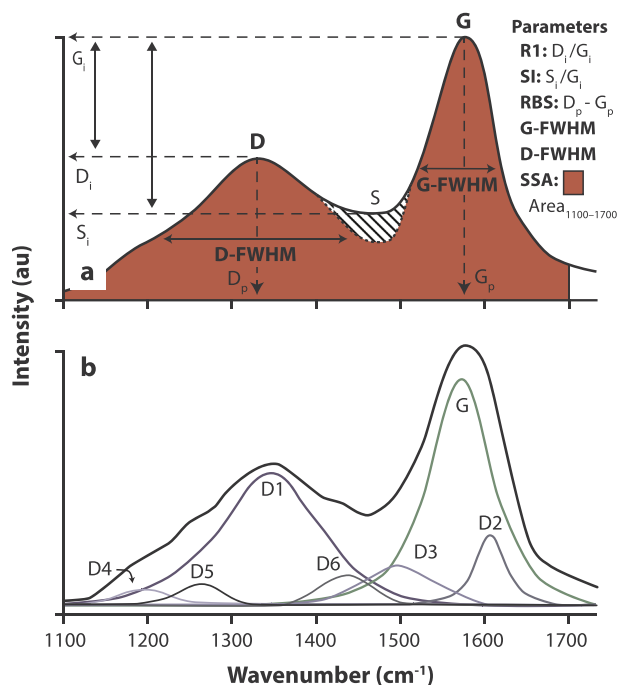
Fig. 2. First-order Raman bands of OM. (a) Non-deconvolved spectrum, along with the Raman parameters that can be calculated. Note that the suffix is 'band' (Table 1). (b) 6-band deconvoluted spectrum with the proposed nomenclature of the bands when performing deconvolution. The suffix 'function' is employed to differentiate deconvoluted bands (Table 1). The number of bands fitted to the spectrum is subject to the operator's discretion; however, it is proposed that the band nomenclature presented here should be followed to avoid confusion. SI – saddle index; RBS – Raman band separation; G-FWHM – G-band/function full-width at half-maximum; D-FWHM – D-band/function full-width at half-maximum; SSA – scaled spectrum area.

Fig. 3. Illustration showing how the second-order region Raman bands of OM change with increasing maturity (ordering). (a–b) amorphous OM. (c–e) ordered graphite.

2017; Henry et al., 2018). The occurrence of the most common additional bands (Fig. 2b) are as follows: D2-band (c. 1610 cm^{-1}); D3-band (c. 1500 cm^{-1}); D4-band (1200 cm^{-1}); D5-band (c. 1260 cm^{-1}) and D6-band (c. 1440 cm^{-1}). The D2-band has been related to the disorder inside the graphitic lattice with E_{2g2} symmetry (Allwood et al., 2006) and is merged with the G-band for low-ordered OM. With increasing maturity, the D2-band evolves, firstly appearing as a small bump on the red-shift shoulder of the G-band until it eventually splits from the G-band and disappears (Buseck and Beyssac, 2014). The D3-band results from the out-of-plane vibration due to defects and heteroatoms, which eventually disappear during graphitization (Wopenka and Pasteris, 1993; Beyssac et al., 2002; Baludikay et al., 2018). The D4- and D5-bands were related to the CH species in aliphatic hydrocarbon chains by Ferralis et al. (2016), as they demonstrated a strong correlation between the atomic H:C ratio and the band properties. The D6-band at c.1440 cm^{-1} was recognised by Romero-Sarmiento et al. (2014), which in their study was termed the D5-band. They proposed that the D6-band is related to the hydrocarbons trapped within the micropores of organic matter. From now on, when we refer to fitted bands after performing deconvolution, they will be followed by the suffix 'function', for example D4-function.

The second-order region (2200–3400 cm^{-1}) has mostly been used for samples that have undergone metamorphism, as the bands are not clearly distinguished for lower maturity samples (Fig. 3). The region has a total of five bands with different evolutionary paths from disordered to ordered OM, and they begin to become identifiable at the anthracite stage (> 2%VR$_o$; Pasteris and Wopenka, 1991; Wopenka and Pasteris, 1993; Cuesta et al., 1994; Spötl et al., 1998; Jehlička and Beny, 1999; Beyssac et al., 2002; Jehlička et al., 2003; Rantitsch et al., 2004; Zeng and Wu, 2007; Liu et al., 2013; Yuman et al., 2018). The most
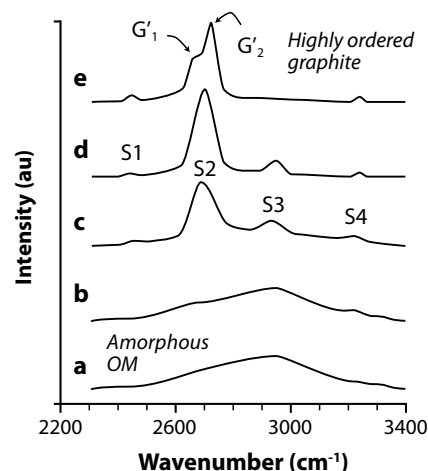
common interpretation of these bands is that they are a mixture of overtones and combinations of different inelastic scattering of the bands in the first-order region (Wopenka and Pasteris, 1993; Beyssac et al., 2002; Childress and Jacobsen, 2017). For example, the S2-band at c. 2700 cm^{-1} is an overtone of the D1-band at c. 1340 cm^{-1} (1340 × 2 = 2680 cm^{-1}), whereas the S3-band at c. 2950 cm^{-1} is a combination of the D1 and G-bands (1350 + 1580 = 2930 cm^{-1}).

There is considerable inconsistency in the nomenclature and positions of the Raman bands used by different authors, and the number of bands used for analysis in both the first- and second-order regions; this leads to confusion when comparing results from different studies, which has inhibited the development of a standardized method. To avoid confusion in future publications, we propose to use the nomenclature described in Fig. 2 and Table 1 for the first-order region and Fig. 3 and Table 2 for the second-order region. The recommended number of bands to include during deconvolution is discussed in Section 5.1.

In the first-order region, the G-band has been referred to the "O" band, which stands for "ordered" (Wopenka and Pasteris, 1993; Spötl et al., 1998; Jehlička and Beny, 1999; Zeng and Wu, 2007; Schiffbauer et al., 2012; Liu et al., 2016) or the "G" band (Cuesta et al., 1994; Kelemen and Fang, 2001; Beyssac et al., 2002), which stands for "graphite", and the latter is a ubiquitous term used in most recent literature. However, Kouketsu et al. (2014) argued that it is not possible to determine the G-band at c. 1580 cm^{-1} for low-grade OM, and therefore called the band at c. 1580 cm^{-1} the "D2" band. Ito et al. (2017) used the D2-band abbreviation to be synonymous with the G-band; other studies have used "G-band" to be a combination of the G- and D2-bands (Henry et al., 2018, 2019). It is noted that the D2-band has been referred to as the D′-band (Marshall et al., 2005; Ammar and Rouzaud, 2012). By contrast, Jubb et al. (2018) located the D2-band position at c. 1520 cm^{-1}, where the D3-band is commonly placed, whereas Song et al. (2019) fitted the D2-band at c. 1700 cm^{-1}, where there is a known carbonyl group (C=O) vibration (Li et al., 2006).

The D1-band at 1350 cm^{-1} was termed the "A" band by Kelemen and Fang (2001), as it represents the "amorphous" structure of the OM. Hu et al. (2015) also used unconventional nomenclature, calling the fitted function at 1336 cm^{-1}, the "D" band (instead of the D1-band) and the function at c.1200 cm^{-1}, the "D1" band (instead of the D4-band). Ferralis et al.'s (2016) D5-band classification was previously used by Romero-Sarmiento et al. (2014), however their D5-band was located at c. 1440 cm^{-1}, rather than c. 1260 cm^{-1}. Ferralis et al. (2016) unconventionally named two bands in the same spectrum, the "D3" band. This lack of consistency is detrimental to the wider use of Raman and creates considerable confusion.

Table 1
Proposed nomenclature for the Raman spectrum in the first-order region.

Method	Proposed nomenclature	Position (cm^{-1})	Alternative nomenclatures	Notes
No deconvolution	D-band	c.1580	A	
	G-band	c.1350	O	
Deconvolution	G-function	c.1580	G_L, O, D2	If D2 is not fitted, assume that the band is a combination of G and D2.
	D1-function	c.1340	D	
	D2-function	c.1610	G_L, O, D2, G	
	D3-function	c.1500	D2	
	D4-function	c.1200		If D4 is fitted, and D5 is not, assume that they are combined.
	D5-function	c.1260		This band is rarely fitted.
	D6-function	c.1440	D3	This band is rarely fitted. Termed differently by Romero-Sarmiento et al. (2014).

We propose that the terminology outlined in Fig. 2 and Table 1 should be adopted for the first-order region of Raman spectra. The general term "D-band" is used for non-deconvoluted spectra; where deconvolution is performed individual D1 – D6 'bands' (functions) can potentially be distinguished (Fig. 2).

For the second-order region, we propose the adoption of the no-menclature summarised in Fig. 3 and Table 2, which follows that used by Spötl et al. (1998), Jehlička and Beny (1999) and Zeng and Wu (2007). For immature samples there is a single broad band, and only with increasing maturity do the S2 (c. 2700 cm^{-1}), S3 (c. 2950 cm^{-1}) and S4 (c. 3200 cm^{-1}) bands become identifiable (Fig. 3; Zeng and Wu, 2007; Pan et al., 2019). Once the OM becomes anthracite and the graphitization process begins, the S2- and S3-bands become more discernible and separate into two clear bands (Fig. 3). Another small peak, termed the S1-band, also becomes visible at c. 2450 cm^{-1} (Buseck and Beyssac, 2014; Pawlyta et al., 2015; Rantitsch et al., 2016). As the graphitization process continues with increasing thermal alteration, the S2-band becomes stronger and the S1, S3 and S4 bands become weaker. In highly-ordered graphite, the S2-band splits into two separate peaks (Fig. 3), called the G′$_1$ (c. 2690 cm^{-1}) and G′$_2$ (2735 cm^{-1}) doublets (Lespade et al., 1982; Wopenka and Pasteris, 1993; Jehlička and Beny, 1999; Beyssac et al., 2002; Rantitsch et al., 2016), which indicate that the OM is changing to a tri-periodic structural organization (Lespade et al., 1982; Cuesta et al., 1994).

4. Raman parameters for different applications

Here, different parameters will be summarised and their suitability for the three main Raman applications: (1) hydrocarbon exploration; (2) metamorphic studies; (3) estimating maximum heating along fault planes, will be assessed. Table 3 lists commonly recommended parameters along with their source references. The parameter values will not be discussed per se in this section, as the values are strongly dependent on the different methodologies applied (Lünsdorf et al., 2014; Henry et al., 2018); we will focus on each parameter's trend and its suitability for each application.

There is considerable confusion concerning parameter abbreviations. For example, Lahfid et al.'s (2010) RA1 and RA2 area ratio parameters were first used to represent the following equations, respectively: (D1 + D4)/(D1 + D2 + D3 + D4 + G) and (D1 + D4)/(D2 + D3 + G). Chen et al. (2017) then used the same abbreviations, RA1 and RA2, to indicate the area ratios of D/G and D2/G respectively. The same abbreviations were used again for different parameters by Schito et al. (2017): RA1 = (S + Dl + D)/(S + Dl + D + Dr. + Gl + G) and RA2 = (S + Dl + D)/(Dr + Gl + G; see Schito et al. (2017) for definitions of their band nomenclature). The RA1 and RA2 Raman parameters sensu Lahfid et al. (2010) are most commonly used in metamorphic studies (Hara et al., 2013; Kouketsu et al., 2014; Lünsdorf et al., 2014; Delchini et al., 2016; Schito et al., 2017); therefore, we propose that these equations and abbreviations should be followed. There are also discrepancies in the definition of the R2 and R3 Raman parameters (Table 3) between Beyssac et al. (2002) and Hu et al. (2015). For these two parameters, we propose following Beyssac et al. (2002), as they are the most widely used (Beyssac et al., 2002; Rantitsch et al., 2004; Mathew et al., 2013; Childress and Jacobsen, 2017).

The R1 and G-FWHM Raman parameters have also been defined in different ways. Depending on how the G-band region is fitted, whether it is a combination of the G- and D2-functions or fitted separately, different names have been used. When the R1 ratio is calculated using the merged G- and D2-functions some have termed it simply the I_D/I_G (Quirico et al., 2005; Nakamura et al., 2019; Schito et al., 2019), whereas others have continued to call it R1 (Eichmann et al., 2018; Henry et al., 2018, 2019). On the other hand, when the G-FWHM is calculated using a combination of the G + D2-functions it has been called the G + D$_2$ width (Eichmann et al., 2018), as well as the G-FWHM (Henry et al., 2018, 2019). We suggest that the R1 and G-FWHM names should continue to be used whether or not the G-band region is separated into the G- and D2-functions; however, operators should be aware that calculating these Raman parameters via the two methods may lead to significant differences in the values obtained.

4.1. Diagenesis, catagenesis and metagenesis

During normal burial conditions, OM remains disordered during diagenesis, catagenesis and metagenesis, as it has not been subject to high enough temperatures to transform into graphite (Fig. 4). During

Table 2
Proposed nomenclature for the second-order region of the Raman spectrum.

Proposed nomenclature	Position (cm^{-1})	Alternative nomenclatures [a]	Notes
S1	c.2450	S5, D + D″, D*, 2D4, 2450 cm^{-1}	This band is often not named and is ignored as data are commonly not collected at < 2600 cm^{-1}.
S2	c.2700	S1, S, 2D, 2′D1, 2D1	The S1 band splits into two individual bands for highly ordered graphite. 2D = overtone of D-band (2 × 1350 = 2700 cm^{-1}).
G′$_1$	c.2685	NA	This band arises when the S2 band splits into two bands for highly ordered graphite.
G′$_2$	c.2735	NA	This band arises when the S1 band splits into two bands for highly ordered graphite.
S3	c.2900	S2, D1 + G, D + G	Combination of the D1 and G bands (1580 + 1340 ≈ 2920 cm^{-1})
S4	c.3180	S3, D + D′, 2D′, 2′D2, G″, 2D2	This band is often ignored as data are not collected at > 3000 cm^{-1}.

[a] see Spötl et al. (1998); Jehlička and Beny (1999); Beyssac et al. (2002); Jehlička et al. (2003); Nestler et al. (2003); Rantitsch et al. (2004); Zeng and Wu (2007); Liu et al. (2013); Nakamura et al. (2015); Pawlyta et al. (2015); Hu et al. (2015); Childress and Jacobsen (2017); Yuman et al. (2018). NA = not applicable.

Table 3
Raman parameters that have been recommended for maturity estimation, along with exemplar studies that have used these parameters.

Method	Parameters	Abbreviations and notes	References
Full width at half maximum (FWHM)	G	G-FWHM	Roberts et al. (1995); Jehlička and Beny (1999); Guedes et al. (2005), Quirico et al. (2005), Yoshida et al. (2006), Guedes et al. (2010), Romero-Sarmiento et al. (2014); Zhou et al. (2014); Nakamura et al. (2015, 2019), Bonoldi et al. (2016); Rantitsch et al. (2016), Henry et al. (2019).
	D1	D1-FWHM	Zhou et al. (2014); Chen et al. (2017).
	D1/G	$D1_{FWHM}/G_{FWHM}$	Spötl et al. (1998); Zhou et al. (2014); Hu et al. (2015); Lupoi et al. (2017); Schito and Corrado (2018); Kaneki and Hirono (2019).
Raman band positions	G – D or G – D1	Raman Band Separation (RBS)	Liu et al. (2013); Zhou et al. (2014); Bonoldi et al. (2016); Schmidt et al. (2017); Jubb et al. (2018); Schito and Corrado (2018); Henry et al. (2019).
Ratio of Raman band height	D/G or D1/G	R1	Roberts et al. (1995); Rantitsch et al. (2004); Jurdik et al. (2008); Liu et al. (2013); Zhou et al. (2014); Nakamura et al. (2015); Lupoi et al. (2017); Sauerer et al. (2017); Childress and Jacobsen (2017); Kaneki and Hirono (2018); Schito and Corrado (2018); Kouketsu et al. (2019b).
	S/G	Saddle Index (SI)	Wilkins et al. (2014); Henry et al. (2018).
Ratio of band areas	D1/G	A_D/A_G	Kribek et al., 1994; Guedes et al. (2005); Zhou et al. (2014); Nakamura et al. (2015); Chen et al. (2017); Schmidt et al. (2017); Schito and Corrado (2018); Mukoyoshi et al. (2018).
	D1/(G + D1 + D2)	R2	Beyssac et al. (2002); Rantitsch et al. (2004); Court et al. (2007); Aoya et al. (2010); Huang et al. (2010); Scharf et al. (2013); Delchini et al. (2016); Nakamura et al. (2015); Rantitsch et al. (2016); Chen et al. (2017); Childress and Jacobsen (2017); Kirilova et al. (2018); Beyssac et al. (2019); Kouketsu et al. (2019b).
	(D1 + D4)/(D1 + D2 + D3 + D4 + G)	RA1	Lahfid et al. (2010).
	(D1 + D4)/(D2 + D3 + G)	RA2	Lahfid et al. (2010).
Total Area	Σ_{Area} 1100–1700 cm^{-1}	Scaled Spectrum Area (SSA) – Scale G-Band to 2000 au.	Henry et al. (2019).
	Σ_{Area} 1000–1800 cm^{-1}	(1) Scaled total area (STA)	Lünsdorf (2016); Hackley and Lünsdorf (2018); Rantitsch et al. (2019).
		(2) Scaled Total Area (D_STA) – normalize to maximum D1 value. (3) Scaled Total Area (G_STA) – normalize to maximum G value.	
Multi-linear regression	Σ_{Area} (1575–1595 cm^{-1}) / Σ_{Area} (1610–1630 cm^{-1})	G_shape_factor	Lünsdorf et al. (2017)
	Uses a multi-linear regression, which include several Raman parameters to construct an empirical relationship with *VR*. See Wilkins et al. (2014, 2015) for further detail.	RaMM (1)	Wilkins et al. (2014, 2015, 2018)
		RaMM (2)	Wilkins et al. (2015, 2018)

FWHM – Full Width at Half Maximum. au – arbitrary units.

catagenesis and metagenesis, important thermal decomposition reactions occur in OM that lead to the generation of oil and gas. It is therefore of no surprise that there has been a tremendous amount of work trying to track the thermal evolution of OM during these stages, particularly to determine the onset of oil, wet gas and dry gas generation (Hartkopf-Fröder et al., 2015). The most common techniques used are vitrinite reflectance (VR$_o$) and Rock-Eval™ pyrolysis.

VR$_o$ is widely used to calibrate basin models that help petroleum exploration geologists delineate areas of interest by creating maturity maps used in common risk segment mapping. It is therefore of value to generate equivalent vitrinite reflectance (%$_{eq}$VR$_o$) values when VR cannot be performed, such as in pre-Devonian and deep marine rocks where vitrinite particles are absent/rare, and when VR is subject to suppression and/or retardation, caused by macerals with high hydrogen concentration (e.g. liptinites, amorphous organic matter and hydrogen-rich vitrinites), different lithologies, and in overpressured basins (Carr, 2000; Hackley and Cardott, 2016). Reflectance data from graptolites, bitumen, chitinozoans and conodonts; thermal alteration indices (TAI)

such as the spore colouration index (SCI); and geochemical techniques such as Rock-Eval™ pyrolysis and biomarkers have all been employed to estimate %$_{eq}$VR$_o$ (Jarvie et al., 2001; Hartkopf-Fröder et al., 2015 and references therein).

Raman spectroscopy has been recently used to determine the %$_{eq}$VR$_o$ of OM in the oil and gas windows (0.6–3.0%VR$_o$; Baludikay et al., 2018; Schito and Corrado, 2018; Henry et al., 2019) from a variety of different organic matter components including vitrinite, graptolites and bitumen. The type of organic matter is not taken into account in Sections 4.1 to 4.3, below, however it will be discussed in Section 5.2. A summary of how the Raman spectrum and Raman parameters evolve with increasing maturity is provided in Fig. 4. Visually, the main changes in the OM Raman spectrum with increasing maturity (increasing VR$_o$), are that the G-FWHM decreases and the distance between the D or D1-band and G-band increases.

The two most successful Raman parameters used to estimate VR in the range of 0.5–3.0%VR$_o$, are G-FWHM (Wopenka and Pasteris, 1993; Spötl et al., 1998; Kelemen and Fang, 2001; Guedes et al., 2010;
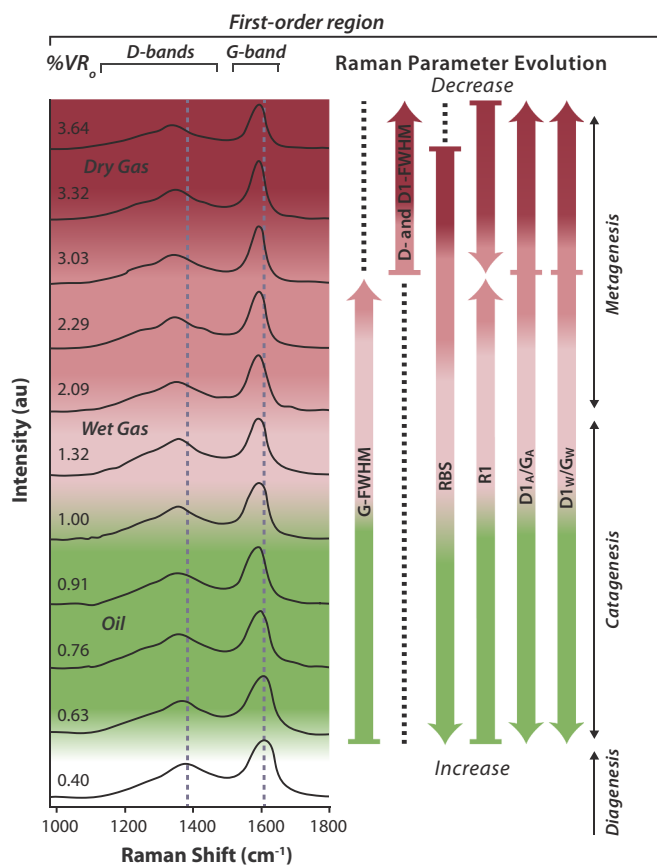
Fig. 4. Summary of how the Raman spectrum of OM and parameters change with increasing VR$_o$. Dashed blue lines indicate the low maturity D-band and G-band peak positions. The dashed black lines for the Raman parameter evolution indicate invariable change in the parameter values. (For interpretation of the references to colour in this figure legend, the reader is referred to the web version of this article.)

Hinrichs et al., 2014; Romero-Sarmiento et al., 2014; Eichmann et al., 2018; Schito and Corrado, 2018; Henry et al., 2019) and RBS (Kelemen and Fang, 2001; Zhou et al., 2014; Inan et al., 2016; Mumm and Inan, 2016; Sauerer et al., 2017; Khatibi et al., 2018a, 2018b, 2018c; Schito and Corrado, 2018) (Fig. 5). It is impossible to compare the absolute values between studies, as the deconvolution methods and Raman set-ups are highly variable. However, Fig. 5 shows that the parameters have a general trend. The G-FWHM parameter (Fig. 5a) has a non-linear relationship with VR$_o$: it sharply decreases from 0.5–2.0%VR$_o$, the gradient reduces to 3.0%VR$_o$, and then flattens out at > c. 3.0%VR$_o$ (Fig. 5). The RBS parameter behaves similarly, rising sharply to c. 2.0–4.0%VR$_o$ and then begins to flatten out (Fig. 5b). This shows that the G-FWHM and RBS are strong parameters to estimate the maturity of source rocks in the oil, wet gas, and dry gas generation stages. However, they cannot confidently be used to estimate the maturity of over-mature petroleum source rocks.

The R1 parameter is commonly used in maturity studies (Table 1), however it is generally considered to be a poor parameter to estimate %$_{eq}$VR$_o$ values in the oil and gas maturity range (Beny-Bassez and Rouzaud, 1985; Lünsdorf et al., 2017; Henry et al., 2019). The R1 value has a three-stage evolution, it: (1) decreases slightly up to c. 2.5%VR$_o$; (2) then increases up to low-grade metamorphism; and (3) sharply decreases for medium- to high-grade metamorphism, until the OM becomes a perfectly-ordered graphite and the disordered band region disappears (Beyssac et al., 2002; Rahl et al., 2005; Lünsdorf et al., 2017) (Figs. 5–7). This trend for the R1 ratio makes assessing the maturity for oil and gas exploration ambiguous, as one R1 value offers three different possible VR$_o$ values; visual inspection of the spectrum is

essential. The R1 parameter is also not as sensitive as G-FWHM and RBS, as small variations of R1 can give substantially different %$_{eq}$VR$_o$ values, and the error associated with the R1 parameter is greater than the subtle decrease of the R1 for the oil and gas generation stages (Fig. 5c). However, these general observations are contrary to the results of Guedes et al. (2010) and Liu et al. (2013), who determined R1 parameter values that increased with increasing maturity up to c. 5.0% VR$_o$ with a steep linear calibration curve, albeit with significantly different values, attributable to the contrasting spectral processing methods used. On the other hand, the R1 results of Muirhead et al. (2017b) demonstrated opposite trends for samples in different localities that have been affected by igneous intrusions, which they proposed to be a result of the different heating rates experienced. This suggests that the R1 ratio may not be suited to determine the maximum temperature, but rather may be used as a means to compare different heating rates.

Studies of the D1-FWHM parameter show conflicting results (Fig. 5d). Some authors have shown that D1-FWHM has little to no use to estimate the maturity of OM for hydrocarbon exploration, as the band-width remains unchanged up to c. 3–4%VR$_o$ (Wopenka and Pasteris, 1993; Spötl et al., 1998), similar results derived from the D-FWHM were obtained by Henry et al. (2019). Other studies have concluded that the D1-FWHM is well suited to estimate maturities that are relevant for hydrocarbon studies, as the D1-FWHM decreases with increasing maturity (Fig. 5d; Cuesta et al., 1994; Hinrichs et al., 2014; Schito and Corrado, 2018). Some workers have used the ratio of the D- or D1-FWHM and G-FWHM, which also has a two-step evolution. It firstly increases rapidly as the G-FWHM decreases in width, and when the G-FWHM becomes invariable (at > 3%VR), the D1-FWHM starts to decrease in width, leading to a sharp decrease in the ratio value (Spötl et al., 1998; Zhou et al., 2014; Henry et al., 2019). The area ratio of the D1-band and G-band (D1$_A$/G$_A$) is a commonly used Raman parameter and has been shown to increase with increasing maturity up to c. 3.0% VR$_o$ (Fig. 5e; Zhou et al., 2014; Sauerer et al., 2017). It then decreases above c. 3.0%VR$_o$ (Zhou et al., 2014).

Other parameters that have been proposed include Wilkins et al.'s (2014, 2015) Raman Maturity Method (RaMM) that utilises two multi-linear regression equations to predict equivalent VR values between 0.4 and 1.2%VR$_o$ (RaMM 1) and 1.0–2.5%VR$_o$ (RaMM 2) using several Raman parameters. Wilkins et al. (2014) demonstrated that the operator does not need to discriminate vitrinite and inertinites, as both yield similar equivalent VR values. They also proposed that this method corrects for the suppression of VR values. Several integrated area Raman parameters that are calculated between wavenumber regions have also proved to be successful and include the SSA (scaled spectrum area; Henry et al., 2018) and the STA (scaled total area), D_STA (D1-band STA), G_STA (G-band STA) and G_shape_factor (Lünsdorf and Lünsdorf, 2016; Lünsdorf et al., 2017; Table 3).

SSA is the total area of the Raman spectrum between 1100 and 1700 cm^{-1} after background subtraction and normalisation using a maximum G-band height value of 2000, and has a linear correlation with vitrinite reflectance up to c.6.0%VR$_o$ (Henry et al., 2019). Lnsdorf and Lnsdorf's (2016) Raman parameters are derived by using an automated iterative random-based curve-fitting approach to determine the optimum baseline characteristics, which is then used to calculate the: STA, which is the scaled total area between the region 1000–1800 cm^{-1}; D_STA, which is the scaled total area when the spectrum is normalized using the maximum D1-band height between 1000 and 1800 cm^{-1}; G_STA, which is the scaled total area when the spectrum is normalized using the maximum G-band height between 1000 and 1800 cm^{-1}. These parameters have a linear relationship with VR up to c. 6.0%VR$_o$, similar to Henry et al.'s (2019) SSA parameter. Lünsdorf et al. (2017) further developed this approach to include the G-shape-factor ratio, which is the area from 1575 to 1595 cm^{-1} divided by the area from 1610 to 1630 cm^{-1}, which helps to combine both the D_STA and G_STA parameters to better determine the temperature of OM across a wider temperature range.
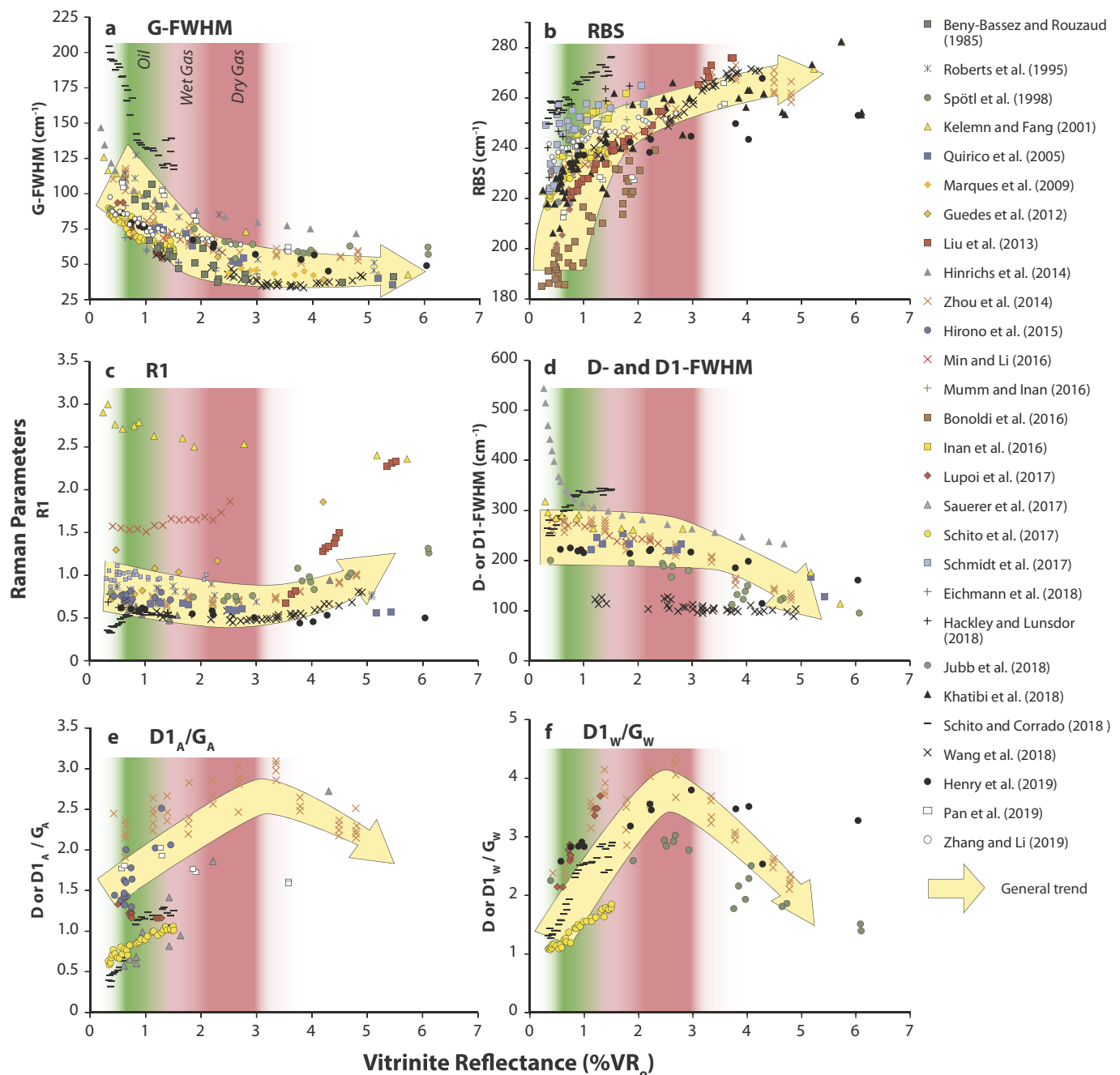
Fig. 5. Raman parameters vs. vitrinite reflectance (VR_o) correlations derived from multiple studies, illustrating the general trend of parameter evolution with increasing VR_o. (a) G-FWHM. (b) RBS. (c) R1. (d) D- or D1-FWHM. (e) D_A or $D1_A/G_A$. (f) D_w or $D1_W/G_W$. Data sources listed in key.

Several authors have proposed that different parameters are more sensitive to different maturity ranges (Liu et al., 2013; Du et al., 2014; Wilkins et al., 2014, 2015; Zhou et al., 2014; Zhang and Li, 2019). Liu et al. (2013) and Zhou et al. (2014) recommended to use both the RBS and R1 Raman parameters: (1) RBS, for low maturity (0.6–3.5%VR_o and 1.5–3.5%VR_o, respectively); and (2) R1 for high maturity OM (3.5–5.5% VR_o and 3.0–5.0%VR_o, respectively). Wilkins et al. (2014, 2015) also developed two separate calibration curves using the RaMM mentioned above, RaMM 1 and RaMM 2. Employing two calibration curves solves the limited range of using one parameter and recognises that different parameters behave differently depending on the maturity. However, the results obtained will be subject to the deconvolution method that is applied.

Understanding the maturity of OM is important for shale gas exploration. Yuman et al. (2018) noted the necessity to recognise over-maturity (> 3.5%VR_o; anthracite) for OM in shale gas reservoirs. The initiation of over-maturity at c. 3.5%VR is a "turning point" for the Raman spectrum and represents a major chemical and structural change for the OM (Hou et al., 2019). This is also broadly demonstrated in Fig. 5 for all the Raman parameters at c. 3.0%VR. In such cases the reservoir quality is severely damaged, as the organic pores and intercrystalline pores of clay minerals are significantly reduced, and source rock quality is poor because the capability to generate hydrocarbons has been exhausted. This is a limiting factor for the two most widely used Raman parameters, G-FWHM and RBS, as they both have non-linear calibration curves that flatten out at c.3.0%VR_o. To address this, Yuman et al. (2018) visually determined the onset of shale gas reservoir deterioration by assessing the appearance of the S2-band in the second-order region. Previously, Liu et al. (2013) had shown that the S2-band starts to appear at c. 3.0%VR_o.
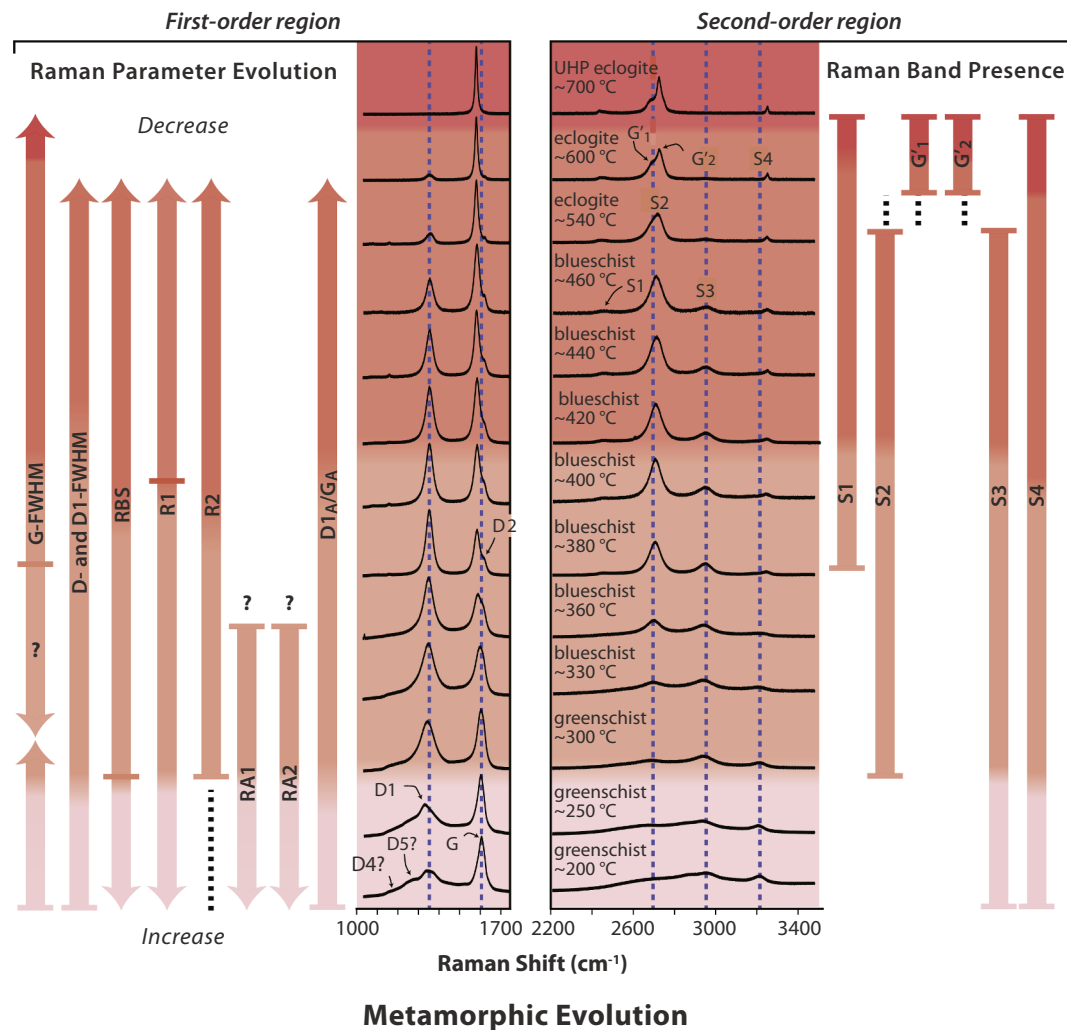
Fig. 6. General evolution of the Raman spectrum of OM for the first-order and second-order regions and changes in Raman parameters with increasing metamorphism. Adapted from Buseck and Beyssac (2014).

In addition to estimating the maturity of OM, several authors have used Raman spectroscopy to determine other properties in the diagenesis to metagenesis burial range. For example, Khatibi et al. (2018a) determined the Young's modulus of OM, using the RBS Raman parameter, which is important to understand the initiation and propagation of fractures during hydraulic fracturing for shale gas production. Romero-Sarmiento et al. (2014) proposed that Raman spectroscopy may have potential to estimate hydrocarbon retention within source rocks, which is a major factor in determining the total resources, by observing what we term the D6-band (c. 1480 cm^{-1}) (Fig. 2c). However, no empirical relationship between hydrocarbon retention and D6-band parameters has been established.

Pan et al. (2019) applied Raman spectroscopy for coalbed methane studies, by determining the deformation of graphite in OM related to the adsorption and desorption of gas in coalbeds, which is important for predicting potential gas outbursts after CO_2 injection (Chen et al., 2009). Pan et al. (2019) demonstrated that after high-pressure gas adsorption and desorption experiments, the OM underwent deformation, which was evident in the Raman spectrum, as the G-band red-shifted, the D1-band blue-shifted and both the FWHM and the $D1_A/G_A$ ratio increased; this suggests that high-pressure gas adsorption and desorption induced defects in the OM lattice.

Wilkins et al. (2018) showed that a RaMM 1 vs. RaMM 2 plot can be used to differentiate bitumen from *Tasmanites*-related alginate. Similarly, Schito et al. (2019) demonstrated that Raman can be used to

identify types of OM particle, using a multivariate Principal Component Analysis (PCA) and Partial Least Square - Discriminant Analysis (PLS-DA) method. They showed that using this approach, sporomorphs and phytoclasts can be differentiated. This application has potential to be taken further and might be used to determine other OM components, which will allow operators to perform high-resolution mapping of OM particles in a sedimentary rock.

To conclude, RBS and G-FWHM remain the most popular Raman parameters employed to determine OM maturity during diagenesis to metagenesis, however they have a limited range of application, up to c. 3.0%VR$_o$ equivalent. Methods that integrate areas of specific Raman regions such as the SSA, G_STA, D_STA parameters correlate well with higher VR values (up to c. 6.0%VR$_o$) and may extend the limited range of RBS- and G-FWHM-based maturity determinations. However, G-FWHM has by far the tightest correlation with VR$_o$ compared to other Raman parameters (Fig. 5; Henry et al., 2019), and should be the method of choice when assessing low-maturity rocks. Nonetheless, we propose that other parameters (RBS, R1, $D1_A/G_A$, integrated area regions) should be calculated to cross-check and extend the G-FWHM results.

4.2. Metamorphism

A substantial number of studies have used Raman spectroscopy as a tool to determine the maximum temperature reached during regional metamorphism (Rantitsch et al., 2004; Endo et al., 2012; Mathew et al.,
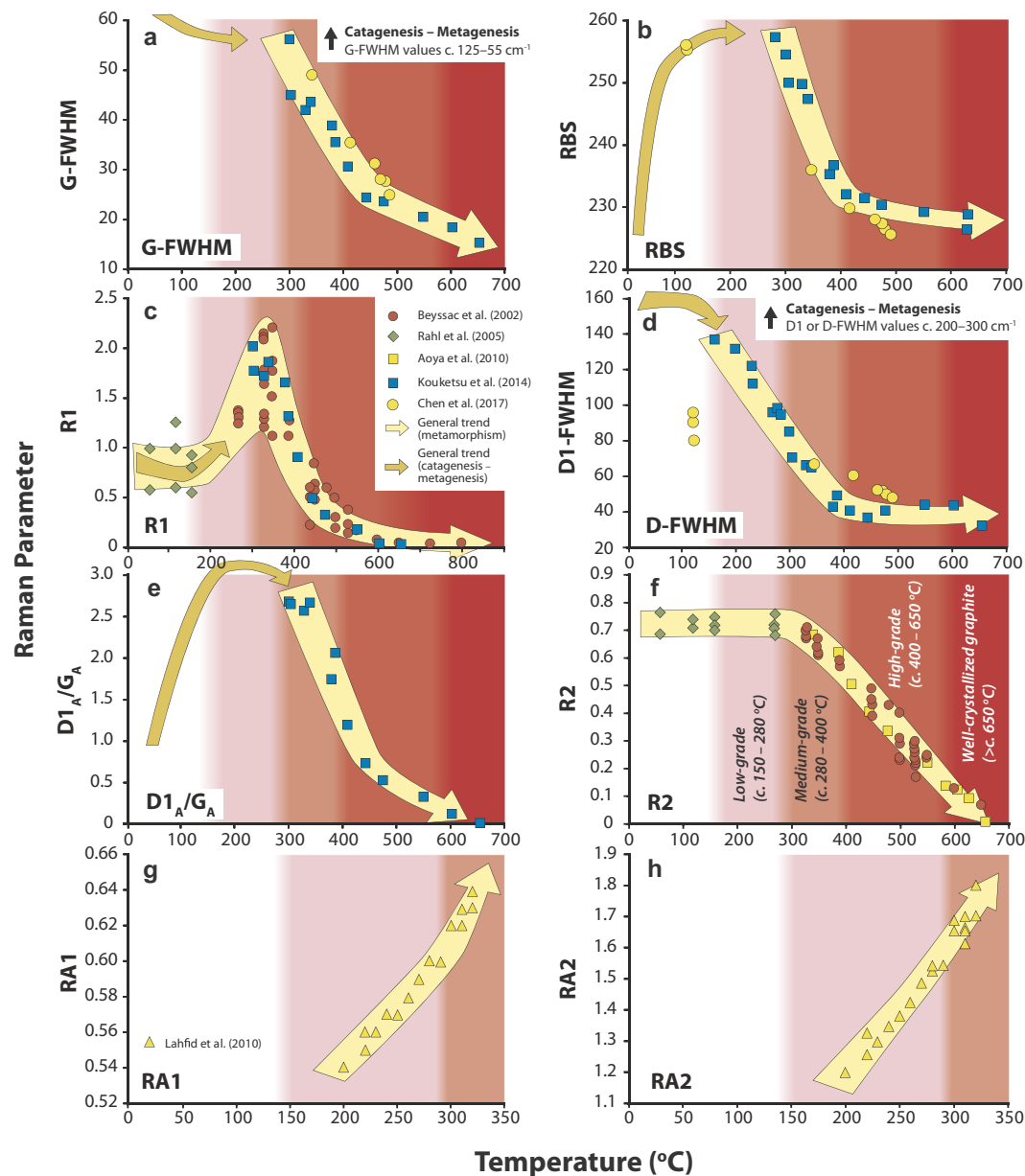
Fig. 7. Raman parameter vs. temperature calibration curves constructed for metamorphic studies. The general trends for metamorphism and catagenesis–metagenesis are shown. The OM crystallinity grade (red shaded bands; key in f) is derived from Kouketsu et al. (2014). (a) G-FWHM. (b) RBS. (c) R1. (d) D1-FWHM. (e) $D1_A/G_A$. (f) R2. (g) RA1. (h) RA2. Data sources listed in key.

2013; Scharf et al., 2013; Buseck and Beyssac, 2014; Muirhead et al., 2017a; Hara and Hara, 2018) or to assess the extent of contact metamorphism due to igneous intrusions (Aoya et al., 2010; Chen et al., 2017; Mori et al., 2017; Henry et al., 2019). Being able to determine the distribution and values of maximum temperatures is extremely important, as it provides insights into the physical and chemical evolution that takes place deep in the Earth, as well as delineating the location of metamorphic facies and minerals that can have substantial economic value. Raman parameters have typically been calibrated against temperature for metamorphic studies, in order to quantify the maximum temperature reached by OM in metamorphic rocks (Figs. 6, 7).

The most widely used calibration curves are presented in Table 4, and a general summary of how the Raman spectrum of OM and Raman parameters change with increasing metamorphism is illustrated in Fig. 6. Examples of Raman parameter vs. temperature calibration curves are shown in Fig. 7. The G-FWHM parameter continues the decreasing trend from diagenesis–metagenesis up to c. 360 °C (Fig. 7a)

and then the D2-band begins to separate from the G-band (Fig. 6; Wopenka and Pasteris, 1993; Buseck and Beyssac, 2014). The D2-band separation transition from the G-band is a possible reason why the G-FWHM has a non-linear calibration curve with VR_o and temperature (°C) values (Kouketsu et al., 2014; Henry et al., 2019), as the G-band FWHM initially begins to widen as the D2-band starts to detached and once it is fully detached, the G-FWHM then decreases again (Fig. 5a).

During catagenesis–metagenesis the RBS parameter increases with increasing temperature and then flattens at $> 3\%VR_o$ (c. 250 °C; Fig. 5b); a reversal occurs during metamorphism and the RBS begins to decrease as the G-band position moves to lower wavenumbers (Figs. 6, 7b), which explains the separation of the D2-band from the G-band. The R1 parameter decreases slightly up to metagenesis, and then R1 begins to sharply increase as the D1/D-band height increases with respect to the G-band height up to c. 350 °C (Fig. 7c); these observations contradict the view of some authors who have stated that the larger the ratio, the less ordered the OM structure Huan et al., 2019. At c. 350 °C, the R1

Table 4
Calibration curves constructed in the literature that have been used for metamorphic rocks.

| Deconvolution (number of bands)	Laser wavelength (nm)	Raman parameters	Calibration eq. T(°C) =	Temperature range (°C) [error]	Reference
G, D1, D2, D3 (4)	514.5	R2	$-445 * R2 + 641$	330–640	Beyssac et al. (2002)
G, D1, D2, D3 (4)	532.2 Nd-YAG	R1 and R2	$737.3 + 320.9 * R1 - 1067 * R2 - 80.638 * R1^2$	100–700 [± 50]	Rahl et al. (2005)
G, D1, D2, D3 (4)	532.2 Nd-YAG	R2	$-(457 \pm 53) * R2 + (648 \pm 25)$	350–550	Rantitsch et al. (2004)
G, D1, D2, D3 (4)	514.5	R2	$221 * R2^2 - 637.1 * R2 + 672.3$	340–655 [± 30]	Aoya et al. (2010)
G, D1, D2, D3 (4)	532	R2	$91.4 * R2^2 - 556.3 * R2 + 676.3$	340–655 [± 30]	Aoya et al. (2010)
G, D1, D2, D3, D4 (5)	514 argon	RA1	NA	200–320	Lahfid et al. (2010)
G, D1, D2, D3, D4 (5)	514 argon	RA2	NA	200–320	Lahfid et al. (2010)
Multiple fitting methods. See Kouketsu et al. (2014)	532 Nd-YAG	D1-FHWM	$-2.15 * (D1\text{-FWHM}) + 478$	150–400 [± 30]	Kouketsu et al. (2014)
Multiple fitting methods. See Kouketsu et al. (2014)	532 Nd-YAG	D2-FWHM	$-6.78 * (D2\text{-FWHM}) + 535$	150–400 [± 50]	Kouketsu et al. (2014)

NA – no available information given in the paper.

ratio displays another reversal (Figs. 6, 7c), and decreases until the D-band region eventually disappears, as the OM evolves to a perfectly ordered graphite.

A number of authors have constructed tailored calibration curves to be used for metamorphic studies, including: Beyssac et al. (2002); Rantitsch et al. (2004); Rahl et al. (2005); Aoya et al. (2010); Lahfid et al. (2010); and Kouketsu et al. (2014) (Table 4). Beyssac et al. (2002) developed the first Raman empirical equation to determine temperatures between 330 and 650 °C, using the R2 parameter (Fig. 7f). The R2 parameter empirical equation was subsequently modified by Rantitsch et al. (2004) who worked on isolated OM and Aoya et al. (2010) who worked on contact metamorphic rocks (Table 4). Endo et al. (2012) and Kouketsu et al. (2014) both tested the Beyssac et al. (2002) and Aoya et al. (2010) R2 calibration equations and demonstrated that the calibration curves showed no significant difference to their results (Fig. 7f). This would imply that the same calibration curve can be used for both regional and contact metamorphism. However, it should be noted that Endo et al., 2012 did not follow the exact method used by Beyssac et al. (2002) or Aoya et al. (2010), as they did not include the D3-band when performing deconvolution. Rahl et al. (2005) tested the R2 parameter for low-grade metamorphic temperatures and showed that R2 remains constant at < 300 °C, and is therefore a poor parameter to quantify low-temperature metamorphism (Fig. 7f). Beyssac et al. (2002) explained that the R2 parameter remains constant below c.300–330 °C because the coherent domains composed by the aromatic rings in the organic matter structure are too small.

Rahl et al. (2005) created a new method combining both the R1 and R2 parameters, to cater for metamorphic rocks that have been exposed to lower temperatures (Table 4, Fig. 8; 100–700 °C ± 50 °C). They successfully tested the calibration equation on low-grade metamorphic rocks in New Zealand and high-pressure metamorphic rocks in Crete (Greece). Rahl et al.'s (2005) wide temperature range offers better practicality, as no prior knowledge of the thermal maturity and geological context is needed. Scharf et al. (2013) tested Rahl et al.'s (2005) equation against those of Beyssac et al. (2002) and Aoya et al. (2010), and showed good consistency for all three methods. However, the Beyssac et al. (2002) and Aoya et al. (2010) calibration curves are in closer agreement with the petrology, especially for higher temperatures (> 500 °C). On the other hand, Mathew et al. (2013) demonstrated that Rahl et al.'s (2005) method better estimates temperatures of < 340 °C and > 600 °C than the approach of Beyssac et al. (2002). Chim et al. (2018) also successfully used Rahl et al.'s (2005) method to determine the metamorphic grade of detritus, to track the uplift and exhumation of an orogenic belt in Eastern Taiwan.

The RA1 and RA2 Raman parameters of Lahfid et al. (2010) also cater for low-temperature metamorphic rocks (Table 4; Figs. 6, 7g, h). Both parameters increase with increasing temperature. Hara et al. (2013)
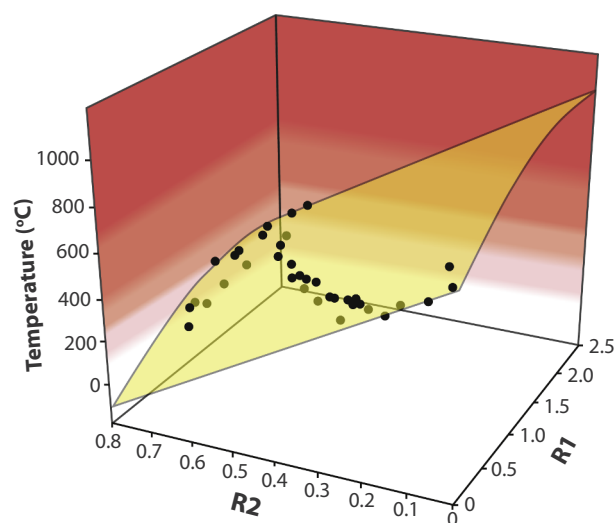
Fig. 8. Calibration data and best fit-surface to determine metamorphic temperature from the R1 and R2 Raman parameters of OM. Adapted from Rahl et al. (2005).

showed that the parameters can reliably estimate low-grade metamorphism (< 300 °C), although Kouketsu et al. (2014) indicated that RA1 and RA2 overestimate the temperature of metamorphic rocks for temperatures < 200 °C and of > 300 °C by > + 50 °C. By contrast, Schito et al.'s (2017) version of the RA1 and RA2 parameters, discussed in Section 4, were successfully applied to low-maturity rocks (0.5–1.5%VR$_o$).

The D1-FWHM parameter of Kouketsu et al. (2014) has been calibrated for the temperature range 150–400 °C (Figs. 6, 7d). The D1-FWHM parameter remains invariable for temperatures > 400 °C. Several authors have applied Kouketsu et al.'s (2014) D1-FWHM Raman method (Baludikay et al., 2018; Hara and Hara, 2018; Mészáros et al., 2019; Yu et al., 2019). For example, Hara and Hara (2018) used it to determine the temperatures reached in an accretionary complex, and Yu et al. (2019) used it to assess the temperature characteristics of detrital graphite particles and employed these as tracers in sediment provenance analysis. Kouketsu et al. (2014) also constructed an empirical relationship with the D2-FWHM parameter and temperature; however, this parameter may prove to be problematic as it is difficult to differentiate between the D2- and G-functions for low-temperature metamorphic rocks (Fig. 6). Nevertheless, Mészáros et al. (2019) utilised the D2-FWHM parameter and got similar results to those obtained using Beyssac et al.'s (2002) and Rahl et al.'s (2005) R2 parameter and

Kouketsu et al.'s (2014) D1 parameter.

Lnsdorf et al.'s (2017) G_STA, D_STA and G_shape_factor have been applied in diagenesis to metagenesis applications (Section 4.1), however, the temperature range of these parameters extend from 160 to 600 °C and they can therefore be used to determine metamorphic temperatures. The SSA parameter by Henry et al. (2018) also extends from 0.5 to 6%VR$_o$, which covers the metamorphic range. Both of these authors' methods derive parameters calculated by integrating area regions (Table 3), and do not use areas of individual bands as is commonly the case for parameters utilised in metamorphic studies (e.g. R2, RA1, RA2).

The second-order region of the Raman spectrum is also helpful for the analysis of metamorphic rocks (Fig. 6; Wopenka and Pasteris, 1993; Buseck and Beyssac, 2014). It is clear from Fig. 6 and from Beyssac et al. (2002) that the height or area ratio of the S2 and S3 peaks can be a powerful parameter, as the S2 height increases with respect to the S3 height with increasing temperature. The splitting of the S2 band into the G′$_1$ and G′$_2$ bands is also a sign that the metamorphic environment has reached extremely high temperatures and pressures (eclogite facies; Beyssac et al., 2002; Buseck and Beyssac, 2014; Rantitsch et al., 2016).

Similar to diagenesis–metagenesis, some authors have tried to use two calibration curves to analyse samples displaying a wide maturity range. Mori et al. (2017) successfully used a combination of Aoya et al.'s (2010) modified R2 equation and Kouketsu et al.'s (2014) D1-FWHM parameter to estimate the maximum temperature reached during contact metamorphism. Their criterion in determining which method to use was whether the D4-band was visibly present or not. If the D4-band was present then the D1-FWHM was used, if not, then the modified R2 parameter was employed. Mori et al. (2017) only used Aoya et al.'s (2010) method close to the intrusion, where the temperatures were high enough for the disappearance of the D4-band.

To summarise, the Raman community studying metamorphism has adopted a more consistent approach than those working on lower maturity rocks (diagenesis to metagenesis), as authors frequently apply and compare calibration curves that have been published in the literature. R2 is the most commonly used Raman parameter albeit calculated following several minor modifications; it appears to offer reliable temperature estimates, with only a small deviation in results obtained by different laboratories. However, the R2 parameter has a limited temperature range and it cannot be employed for low-temperature metamorphic studies (< 300 °C), which is where Rahl et al.'s (2005) and Lahfid et al.'s (2010) Raman parameters can be used. Additionally, Lünsdorf et al. (2017) and Henry et al. (2018) have demonstrated that the integrated areas of specific regions on a smoothed, background-corrected spectrum (rather than individual bands areas), have good linear relationships with temperature and VR$_o$, and the parameters derived from these also have potential application in studies of low- to high-temperature metamorphism. There is therefore scope to unify several methods in order to determine metamorphic temperatures for a wide temperature range.

4.3. Frictional heating along fault zones

Determining the maximum temperature reached during frictional heating along fault planes can provide important information on the amount of total seismic energy released, shear stress, slip distance and the mechanochemistry (Kitamura et al., 2012; Kaneki et al., 2016; Kaneki and Hirono, 2018, 2019). Understanding the maximum temperature along a fault plane can also help predict potential future risks, as the formation of graphite will lead to the lubrication of faults, similar to clays, and magnify the movement along the fault (Oohashi et al., 2011; Kaneki and Hirono, 2018; Kuo et al., 2018).

Measuring the maximum temperature reached on fault planes has typically been performed using vitrinite reflectance (Furuichi et al., 2015; Kaneki et al., 2018). However, Kitamura et al. (2012) argued that VR cannot accurately estimate maximum temperature in a fault zone, as

the mechanochemical effects that are associated with faulting lead to the overestimation of %VR$_o$ maturity. By contrast, Nakamura et al. (2015) proposed that shearing during faulting leads to interlayer delamination and pulverization of OM, increasing edge plane defects and therefore lowering the crystallinity of OM, leading to an underestimation of maturity. On the other hand, it has been suggested that Raman spectroscopy may provide information on both the maximum temperature reached and the deformation processes, unlike vitrinite reflectance (Nakamura et al., 2015; Kaneki et al., 2016; Kaneki and Hirono, 2018; Kuo et al., 2018).

Raman spectroscopy has been used in multiple studies in order to measure the maturity of OM in fault zones and there is clear evidence that the Raman spectra in pseudotachylytes, cataclasites and host rocks are different (Furuichi et al., 2015; Nakamura et al., 2015; Kaneki et al., 2016; Liu et al., 2016; Ito et al., 2017; Kouketsu et al., 2017; Kuo et al., 2017, 2018; Kaneki and Hirono, 2018; Mukoyoshi et al., 2018). The calibration curves constructed to estimate the thermal maturity of burial and contact metamorphism cannot be applied here, as there are other important factors that must be taken into consideration, such as: heating rates; duration of heating; slip rate; shearing; repeated heating episodes; and interaction with hydrothermal fluids. Different laboratory experiments have been performed in order to understand some of these effects, however it is very hard to replicate natural conditions in the laboratory and create reliable calibration curves (Hirono et al., 2015; Kaneki et al., 2016; Kaneki and Hirono, 2018; Mukoyoshi et al., 2018; Nakamura et al., 2019).

The D1$_A$/G$_A$ and R1 parameters are most commonly used to estimate frictional heating in fault zones. Fig. 9 shows how the D1$_A$/G$_A$ and R1 parameters evolve with increasing frictional heating. D1$_A$/G$_A$ values remain relatively constant at < 300 °C although some authors have shown that they decrease slightly (Kaneki et al., 2016; Mukoyoshi et al., 2018), then begin to increase up to 1000 °C (Fig. 9a). Beyond 1000 °C, D1$_A$/G$_A$ values begin to decrease. This is a similar trend to that observed during diagenesis–metagenesis and metamorphism (Fig. 7e), albeit at substantially different temperatures. The R1 ratio remains constant at < c. 700 °C and then begins to increase (Fig. 9b). However, unlike diagenesis–metagenesis and metamorphism, the ratio continues to increase to 1300 °C. It could be that the R1 ratio will decrease at higher temperatures.

Hirono et al. (2015) demonstrated that shearing at < 250 °C does not influence the R1 ratio. Kaneki et al. (2018) confirmed that shearing does not impact the R1 parameter at lower temperatures (< 700 °C), but they showed that at elevated temperatures > 700 °C, increased shearing pressures progressively increases the R1 ratio, as the increasing temperature allowed the formation of graphite that encourages even more shearing. This suggests two things: (1) Hirono et al.'s (2015) shearing experiment did not reach high enough temperatures to promote graphitization and encourage slippage; and (2) the formation of graphite promotes shearing that leads to increased interlayer delamination and pulverization, that has a direct impact on the R1 ratio. Therefore, the R1 parameter may potential be used to determine deformation processes, such as shearing pressures. Results from Kuo et al. (2018) demonstrated that for natural samples, the R1 ratio decreases in the gouge zones, in comparison with the less deformed brecciated zones, which is in disagreement with the experimental results of Kaneki et al. (2018). They also showed that the G-band position red-shifts with increasing strain during faulting. Kuo et al. (2018) also determined that D1-FWHM decreases with respect to the G-FWHM, with increasing frictional heating.

Hirono et al.'s (2015) heating experiments showed that the environmental conditions may potential lead to different types of reactions affecting the Raman parameters, as the D1$_A$/G$_A$ and R1 values for samples heated in air vs. argon were slightly different (Fig. 9). Kaneki and Hirono (2018) demonstrated that faster heating rates in the laboratory delayed the thermal alteration reactions of OM (Fig. 9) and proposed that such delays may also be present in fault rocks.
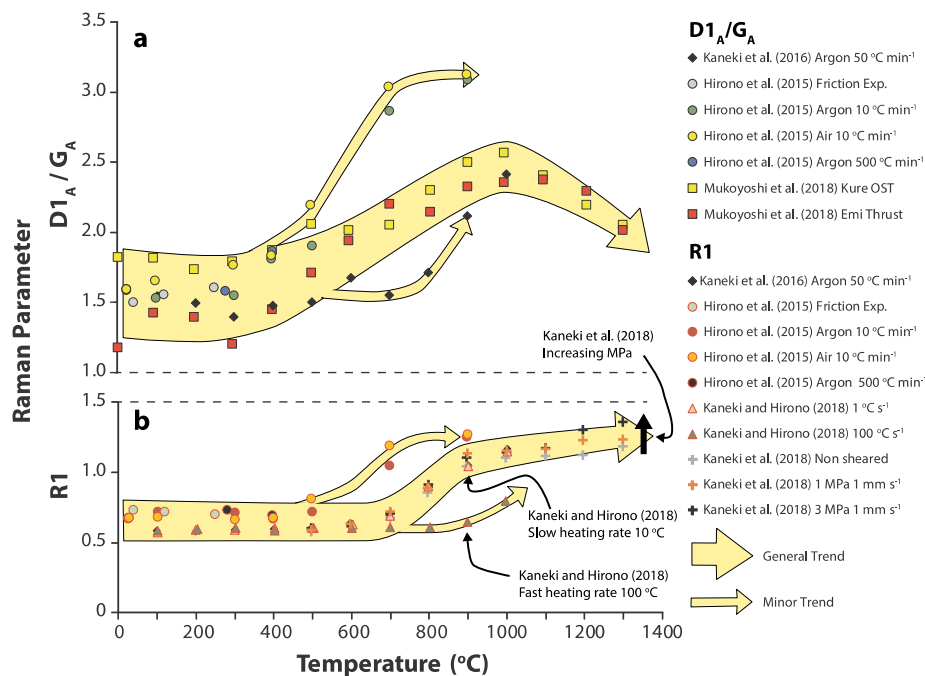
Fig. 9. Trends of Raman parameters with increasing temperature due to frictional heating of OM along fault planes. (a) $D1_A/G_A$. (b) R1. Data sources in the key.

The laboratory experiments performed by Kaneki and Hirono (2019), demonstrated that with increasing maturity the carbonaceous matter weakens and has lower peak friction coefficients, hence promoting slippage. Interestingly, they observed that shearing increases the maturity for low to intermediate maturity carbonaceous matter, whereas shearing decreases the maturity of high-maturity carbonaceous matter. This further highlights the complexity of using Raman as maturity tool in fault zones.

Overall, the study of OM in fault zones using Raman spectroscopy is still in its infancy, and only the $D1_A/G_A$ and R1 parameters have been widely used in the literature. It is recommended that Raman parameters that are not derived from complex deconvolution methods should be tested, in order to minimise bias, similar to the approaches adopted by Lünsdorf and Lünsdorf (2016), Henry et al. (2018, 2019) and Schito and Corrado (2018). Studying graphite in fault zones has an inherent risk, as the carbon needed for graphite formation can originate directly from sedimentary organic matter or from non-organic carbon precipitated from carbon-rich fluids (CO_2 and CH_4; Cao and Neubauer, 2019 and references therein), hence why it is often referred to as 'carbonaceous materials' (CM) in fault zone studies. Unlike vitrinite reflectance, Raman spectroscopy may be able to differentiate between the different origins by using methods that have been previously applied by Wilkins et al. (2015) and Schito et al. (2019) to determine different types of OM. Another limitation in determining the frictional heating of OM in fault zones is that structural ordering may also be induced by the increased pressures and shearing during the physical movement of faults, which has been shown to alter the Raman spectrum (Huang et al., 2010; Kaneki et al., 2018; Kouketsu et al., 2019b).

5. Developing a standardized approach

5.1. Deconvolution

Deconvolution allows the operator to fit multiple functions to the Raman spectrum that represent different modes of vibration and to assess a suite of derived parameters (Beyssac et al., 2002; Wilkins et al., 2014; Sauerer et al., 2017; Schito and Corrado, 2018). Deconvolution is typically performed in the first-order region; however, several studies have also performed it in the second-order region (Beyssac et al., 2002;

Rantitsch et al., 2004; Zeng and Wu, 2007; Childress and Jacobsen, 2017). The number of functions fitted when performing deconvolution in the first-order region is extremely variable, ranging from 2 to 10 functions (Table 5). This lack of consistency between authors makes it near impossible to compare results and biases.

We recommend that simplicity and consistency is key for the wider utilisation of Raman spectroscopy as a geothermometer. However, performing a simple 2-band deconvolution of only the D1- and G-band (Kaneki et al., 2016; Liu et al., 2016; Mukoyoshi et al., 2018; Pan et al., 2019) generates a poor fit with the raw spectra, especially for amorphous OM. Performing complex deconvolution methods with several fitted bands can also be highly subjective and create considerable bias, especially for low-maturity OM (Hinrichs et al., 2014; Lünsdorf et al., 2014; Lupoi et al., 2017; Henry et al., 2018). Some authors have performed several different types of deconvolution depending on how mature the OM is (Kouketsu et al., 2014; Ulyanova et al., 2014; Delchini et al., 2016; Schito et al., 2017); this requires visual identification of the spectra or prior knowledge regarding the burial of the samples. Nevertheless, the use of multiple deconvolution methods for different maturities is essential because with progressive maturation, individual disordered bands will begin to disappear and must be excluded from the deconvolution (Kouketsu et al., 2014; Delchini et al., 2016; Lünsdorf et al., 2017; Schito et al., 2017).

A major talking point is whether to fit the D2-band or not, in the G-band region. Kouketsu et al. (2014) claimed that the G-band is absent for low crystallinity OM ($< 165 \pm 35\,°C$), and that the region at $c.1600\,cm^{-1}$ is composed solely of the D2-band. Only for higher crystallinity samples did they begin to fit the G-band. Several authors have highlighted the difficulty in fitting the D2-band for low maturity/poorly ordered OM (Beyssac et al., 2002; Brolly et al., 2016; Henry et al., 2018). Henry et al. (2018) avoided fitting the D2-band as there is no logical way in determining how the D2 or G-functions should fit. We continue with this school of thought and recommend that if deconvolution is performed, the D2-band should not be fitted, unless it is visible.

Several authors have set constraints when performing deconvolution (Kouketsu et al., 2014; Lünsdorf and Lünsdorf, 2016; Ito et al., 2017). Assigning constraints to peak widths, positions and heights is not advisable, as it forces the deconvolution outcome to work around the conditions that have been set, which may not be representative of the

Table 5
Raman spectral deconvolution methods used in the first-order region for the determination of OM maturity.

Bands (total bands)	References	Notes
No deconvolution	Spötl et al. (1998); Jehlička and Beny (1999); Inan et al. (2016); Henry et al. (2018); Kaneki and Hirono (2019).	
G, D1 (2)	Beny-Bassez and Rouzaud, 1985; Kelemen and Fang (2001); Quirico et al. (2005); Bonal et al. (2007); Zeng and Wu (2007); Liu et al. (2013); Hinrichs et al. (2014); Wilkins et al. (2014); Kaneki et al. (2016); Liu et al. (2016); Schmidt et al. (2017); Kaneki and Hirono (2018); Mukoyoshi et al. (2018)	
G, D1, D2 (3)	Court et al. (2007); Endo et al. (2012); Delchini et al. (2016); Kouketsu et al., 2019b.	
G, D1, D3, D4 (4)	Allwood et al. (2006); Eichmann et al. (2018); Nakamura et al. (2019).	
G, D1, D2, D3 (4)	Beyssac et al. (2002, 2003, 2019); Rantitsch et al. (2004); Marques et al. (2009); Aoya et al. (2010); Huang et al. (2010); Schiffbauer et al. (2012); Zhou et al. (2014); Nakamura et al. (2015); Chim et al. (2018)	
G, D1, D2, D4 (4)	Jubb et al. (2018)	
D1, D2, D3, D4 (4)	Ito et al. (2017); Kouketsu et al. (2017)	
G, D1, D2, D3, D4 (5)	Lahfid et al. (2010); Kouketsu et al. (2014); Bernard et al. (2015); Delarue et al. (2016); Delchini et al. (2016); Chen et al. (2017); Chesire et al. (2017); Childress and Jacobsen (2017); Kouketsu et al. (2017); Nakamura et al. (2017); Sauerer et al. (2017); Baludikay et al. (2018); Golubev et al. (2019); Song et al. (2019)	
G, D1, D2, D3, D4, D5 (6)	Romero-Sarmiento et al. (2014)	
G + D2, D3 (x2), D4, D5	Ferralis et al. (2016)	Ferralis et al. (2016) interpreted two separate D3 bands (c. 1400 cm^{-1} and c. 1500 cm^{-1}) when performing deconvolution.
G, D, + 4 bands (6)	Guedes et al. (2010)	
G, GI, Dr., D, DI, S	Schito et al. (2017)	
8 band	Schopf et al. (2005)	
G_L, G, G_R, V_L, V_R, D, S_L, S, S_R, R (10)	Li et al. (2006); Li (2007); Guedes et al. (2012); Zhang and Li (2019)	Descriptions of what each band signifies is given in Li et al. (2006)
G, D2, D3, D, Sl, S (6)	Bonoldi et al. (2016)	

true nature of the Raman spectrum. On the other hand, it is understood that assigning constraints limits the number of potential deconvolution outcomes for a spectrum. Schopf et al. (2005) considered the best deconvolution outcome to have the best statistical fit with the original spectrum. Although statistical fit is important, operators should not fall into the trap that "if I have a good statistical fit, I have a realistically fitted spectrum", as Henry et al. (2018) demonstrated that functions fitted with unrealistic positions, widths and heights can nonetheless yield good statistical fits. It is therefore recommended that if deconvolution is performed, visual analysis of the spectrum should be undertaken in order to quality check the position, widths and heights of the fitted functions.

When performing deconvolution, Lünsdorf et al. (2017) determined three sources of bias: (1) operator bias; (2) sample heterogeneity bias; (3) different analytical conditions. They proposed that performing an automated method will rule out the operator bias. Several authors have developed an automated deconvolution method in order to determine maturity parameters from individual Raman bands (Lünsdorf and Lünsdorf, 2016; Bonoldi et al., 2016; Schito and Corrado, 2018). Lünsdorf et al. (2017) developed a robust open source software package (http://www.sediment.uni-goettingen.de/download/) that automatically performs random curve fitting in an iterative approach in order to determine the optimum baseline correction, which avoids operator bias. Although deconvolution is performed during the iterative curve fitting steps, the individual bands are not used; it is only used to determine the optimum smoothed, baseline corrected spectrum, where the D_STA and G_STA parameters are calculated. This method has proved to be very successful and the parameters have a good relationship with VR. Lnsdorf et al.'s (2017) method tackles a very important issue, as the baseline correction can introduce extremely bias, the method also avoids using individual bands and uses the area ratios of the whole smooth, baseline corrected spectrum.

Henry et al. (2018) also used a smooth baseline corrected spectrum, however here the baseline is calculated using predefined control points and the accuracy of the baseline correction is determined by performing a visual inspection. This can create unnecessary bias in spectra with a non-linear fluorescence background. In order to avoid bias, Henry et al. (2018) rejected all spectra with substantial fluorescence. Schito and Corrado (2018) also developed a novel approach, where a linear baseline subtraction occurs at the shoulder points of the D1- and G-bands, and then after the baseline correction is performed, each band is fitted with a Gaussian fit separately. This method again tries to minimise the bias associated with the baseline correction, similar to Lünsdorf et al. (2017), but takes a different approach.

A major barrier for the wider utilisation of Raman spectroscopy as a geothermometer, is to decide whether to perform deconvolution or not, as there are many different approaches and it is confusing for a new operator to determine which method to use. In order to encourage the wider use of the technique, Raman spectroscopy needs to be standardized. This review acknowledges that deconvolution has been extremely popular, but it is not an exact science for poorly ordered amorphous OM. Recent papers (Lünsdorf et al., 2017; Henry et al., 2018, 2019; Schito and Corrado, 2018; Mi et al., 2019) have now demonstrated that complex, ambiguous deconvolution methods of several bands are not needed, and that reliable results can be achieved otherwise. Lünsdorf et al. (2017) and Schito and Corrado (2018) have also developed novel approaches to reduce the operator bias in baseline subtraction. We believe that there is no need to perform deconvolution if several Raman parameters (e.g. RBS, G-FWHM, SI, R1, SSA) can be derived from an un-deconvolved spectrum that can track the thermal evolution of OM. This will allow for a more practical and faster analysis with less bias.

5.2. Sample type

Several different sample types have been tested using Raman spectroscopy to analyse OM: polished rock cut-surfaces and thin-sections (Beyssac et al., 2003; Rahl et al., 2005; Allwood et al., 2006; Quirico et al., 2011; Mathew et al., 2013; Hinrichs et al., 2014; Wilkins et al., 2014; Henry et al., 2018), strew slides (Schmidt et al., 2017; Baludikay et al., 2018; Henry et al., 2018; Khatibi et al., 2018a) and rock chips (Muirhead et al., 2017a; Sauerer et al., 2017; Henry et al.,

2019).

It is widely acknowledged that polishing OM can alter the Raman spectrum (Beyssac et al., 2003; Ammar and Rouzaud, 2012; Lünsdorf, 2016; Henry et al., 2018). Results from Ammar and Rouzaud (2012), Lünsdorf (2016) and Henry et al. (2018) showed that polishing increases the relative height and blue-shifted the D1/D-band region. This has been attributed to the interlayer delamination of the carbon structures leading to the buckling of graphene layers (Ammar and Rouzaud, 2012; Lünsdorf, 2016), similar to that observed during frictional heating, as described by Nakamura et al. (2015).

Ammar and Rouzaud (2012) and Henry et al. (2018) demonstrated that after polishing OM with a 1 μm diamond and 0.04 μm colloidal silica slurry respectively, the D1-band region increases in height (increasing the R1 ratio), but the G-FWHM is invariable, suggesting that the G-FWHM parameter has the potential to be used on polished sections. This is valuable information, as polishing a sample may be the only way to locate rare dispersed OM in a rock, and knowing which Raman parameters may or may not be impacted by polishing is essential. Henry et al. (2018) further demonstrated that the change in the D1-band height is not systematic, so it cannot be assumed that polishing impacts all the OM components in a sample to the same degree. This challenges the assumption by Jubb et al. (2018) that polishing impacts all the OM structure by the same amount in a single sample. Lünsdorf, 2016 showed that polishing using a slurry with a grain size of P2500 to 1 μm does not alter the STA, R1 and position of the G-band; however, using a finer grain slurry of 0.05 μm does alters these parameters. Their results indicated that the D1-band decreases in height with polishing, which is the opposite of the results obtained by Ammar and Rouzaud (2012) and Henry et al. (2018) which showed increased values. Lünsdorf (2016) also demonstrated that after polishing the G-band position tends to red-shift for lower maturity samples (c. < 3.0%VR$_o$) and blue-shift for high maturity samples (> 4.0%VR$_o$). The red-shift of the G-band after polishing for low-maturity samples was not observed by Henry et al. (2018). Ammar and Rouzaud (2012), Lünsdorf (2016) and Henry et al. (2018) targeted polished OM; however, authors who have studied polished thin sections have avoided analysing polished OM, by targeting OM that lies beneath the surface of transparent minerals (Pasteris, 1989; Beyssac et al., 2002; Aoya et al., 2010; Ammar and Rouzaud, 2012; Mathew et al., 2013; Kouketsu et al., 2014; Barzoi, 2015; Mészáros et al., 2019).

Analysis of OM in strew slides has been performed by Schmidt et al. (2017) and Henry et al. (2018) by isolating the OM from the rock using hydrofluoric (HF) and hydrochloric (HCl) acids. Both groups recognised the potential of performing palynofacies and multiple thermal alteration studies (e.g. thermal alteration indices, spore colouration index) contemporaneously, along with the Raman analysis. Performing Raman analysis on strew slides is also extremely useful if a rock is lean in OM and locating OM particles via polished sections or in rock-chips proves to be challenging. Schmidt et al. (2017) compared the results derived from translucent, degraded, opaque and bitumen particles, and showed translucent phytoclasts to be the most reliable. Henry et al. (2018) confirmed that opaque phytoclasts should be avoided, but that the Raman parameter results were similar for amorphous organic matter (AOM) and translucent phytoclasts; however, it should be noted that their study was performed on samples with similar low maturity. Lünsdorf et al. (2014) demonstrated another advantage of using strew slides, as treating samples with hydrofluoric (HF) acid lowered the standard deviation for both the RA1 and RA2 parameters; the reason for this was believed to be that the HF removed functional groups or clays, which led to a reduction in the background fluorescence.

It is important to prepare strew slides in a consistent manner and to then store them in a desiccator; however, for long term storage it may be best practice to store them in an inert atmosphere to avoid hydration and oxidation reactions. Schopf et al. (2005) showed that when the same isolated OM particle was dehydrated and hydrated, the G-FWHM values varied by 18 cm^{-1}, which would give significantly different and potentially misleading maturity results. Quirico et al. (2005) highlighted that moisture in the OM can lead to photo-oxidation of the OM which increases the fluorescence. To avoid the fluorescence caused by moisture, Lupoi et al. (2018) dehydrated their samples at 110 °C overnight in an oven prior to Raman analysis. This is inadvisable, as heating a sample at > 60 °C can artificially thermally alter the OM. When preparing strew slides for Raman analysis, we propose that the strew slides should be left to either air dry or oven dry at temperatures < 60 °C for up to 24 h, in order to remove the moisture, and then kept in a desiccator or, if stored for a longer period of time, sealed in an inert atmosphere. Sealing the samples without firstly drying them can lead to continuing oxidation, as the moisture will not have been removed and will persist in the OM (Quirico et al., 2005).

Sauerer et al. (2017) and Henry et al. (2019) demonstrated that the Raman analysis of OM in unprepared rock-chips can be rapid, cheap and reliable; however, it may be difficult to locate OM particles under the microscope, especially for rocks lean in OM. The operator also needs to be careful that adjacent minerals do not produce significant fluorescence, which can obscure the OM Raman bands. Nevertheless, using rock-chips allows Raman spectroscopy to be used on-site, as no sample preparation is needed. However, this approach will work best on coal samples, rather than rocks with dispersed OM.

Brolly et al. (2016) showed that oxidation of rocks can dramatically impact the spectrum of OM, as haematite has a strong Raman band at c. 1300 cm^{-1}, which merges with the D-band region for OM. The presence of haematite will impact the D-band region by shifting the band to lower wavenumbers, reducing the width and increasing the height with respect to the G-band. The G-band is affected, as haematite increases the G-FWHM and blue-shifts the position. Haematite also drastically increases the noise of a Raman spectrum of OM. However, Brolly et al. (2016) showed that treating oxidised samples with HF will remove the interfering haematite signal, as well as removing fluorescence caused by clay minerals (Villanueva et al., 2008; Lünsdorf et al., 2014).

Wopenka and Pasteris (1993) expressed caution regarding the effects of the orientation of OM with respect to the incident laser, as it might potential lead to bias in the results. This is a common phenomenon when performing vitrinite reflectance and is known as bi-reflectance (Hartkopf-Fröder et al., 2015). Aoya et al. (2010) tested this by analysing thin sections that were cut perpendicular and parallel to bedding and demonstrated that the orientation of the elongated OM grains has an insignificant effect when using the R2 Raman parameter for metamorphic rocks in the temperature range 300–650 °C. However, Lünsdorf et al. (2014) revealed that for highly crystalline samples, the structural orientation of the OM with respect to the laser can impact the R1 and R2 ratio. Kouketsu et al. (2014) also noted that the orientation of high crystallinity samples could potentially have a dramatic effect on the Raman spectrum; however, they demonstrated that this effect is negligible for low-temperature/low-crystallinity samples. Tunistra and Koenig (1970) expressed concern about intra-grain heterogeneity, and showed that the Raman spectra close to grain boundaries were different when compared to the spectra acquired from the internal body of the OM. Aoya et al. (2010) therefore proposed that at least 50 measurements should be performed in order to capture this heterogeneity and get reliable average results; this was further highlighted by Lünsdorf et al. (2014).

Kelemen and Fang (2001), Bonoldi et al. (2016) and Schito and Corrado (2018) showed that the thermal evolution of different kerogen types (I, II and III) follow similar trends. Raman spectroscopy has also been performed successfully on different OM components, including bitumen (Liu et al., 2013; Hackley and Lünsdorf, 2018), graptolites (Inan et al., 2016; Mumm and Inan, 2016), chitinozoans (Roberts et al., 1995) and agglutinated foraminifera (McNeil et al., 2016). Mori et al. (2017) demonstrated that Raman parameters derived from OM in limestones, sandstones and mudstones are similar, indicating that lithology does not affect the Raman spectrum. This suggests that Raman measurements may not be impacted by suppression, unlike vitrinite

reflectance.

5.3. Raman instrumentation

It is accepted that different laser wavelengths impact the Raman D-band region of OM (Vidano et al., 1981; Ferrari and Robertson, 2001; Starkey et al., 2013; Sauerer et al., 2017; Henry et al., 2018; Jubb et al., 2018). There is a progressive red-shift of the position of the D-band region with increasing excitation wavelength and vice-versa, whereas the position of the G-band remains unaffected (Vidano et al., 1981; Kouketsu et al., 2014; Jubb et al., 2018). Aoya et al. (2010) compared the R2 parameter values from a 514.5 nm and a 532 nm laser and demonstrated that the 532 nm laser had systematically slightly larger R2 values. Starkey et al. (2013) demonstrated that increasing the laser wavelength from 473 nm to 632 nm, increases the D1-FWHM, whereas the G-FWHM have very similar values using a 473 nm and 514 nm system and only increases greatly when using a laser wavelength > 632 nm. They also showed that the D1-band position blue-shifts and that the G-band position unpredictably changes with increasing laser wavelength. Visual inspection of the spectra in Starkey et al. (2013), suggests that the G-band height decreases with respect to the D1-band height with increasing wavelength, which has also been demonstrated by Lünsdorf and Lünsdorf (2016). D1-FWHM and G-FWHM results obtained by Kouketsu et al. (2014) showed little difference between the 514.5 nm and 633 nm lasers, whereas the D1-band position and R1 ratio were affected; however, they did not show any data that describes how these parameters are affected. Lünsdorf et al. (2017) demonstrated that the D_STA and G_STA parameters follow the same path with increasing maturity when using either a 488 nm or a 532 nm laser.

Current evidence suggests that the G-FWHM parameter may have good comparability between laboratories using different laser wavelengths and any differences will be related mostly to operator bias. By contrast, D1-FWHM, RBS and R1 values will be impacted by both the choice of laser wavelength and operator bias. Increasing the laser wavelength will also increase fluorescence and drastically reduce the quality of the Raman spectrum (Quirico et al., 2005; Lünsdorf and Lünsdorf, 2016; Henry et al., 2018; Goryl et al., 2019). It is therefore recommended to use a laser wavelength < 532 nm, especially for low-maturity samples.

An interlaboratory experiment consisting of three laboratories was performed by Lünsdorf et al. (2014), who showed that the R1 and R2 results can be significantly different, even if the same laser wavelength is used. The disparity in the results may be attributed to other factors such as different gratings and CCD cameras, intra-sample heterogeneity and most importantly, operator bias. Further comparisons between different Raman spectroscopy setups will be essential to see whether laboratories can use the same calibration curves or not, and to determine which setups inherently generate the least bias.

Henry et al. (2018) demonstrated that in-situ burning of OM occurs when using a laser power > 1 mW and this causes increased fluorescence in the Raman spectrum, as well as blue-shifting the G-band position and increasing the G-FWHM. Whereas the D-band region, other than being affected by fluorescence, remains invariable. This has subsequently also been shown by Nakamura et al. (2019). It is therefore advised that low laser powers are used (c. 0.02 mW) and inspection before and after the analysis should be performed to determine whether any damage has occurred (Henry et al., 2018).

5.4. Calibration

Raman studies on OM to date have been performed in a large number of laboratories world-wide by teams of researchers using different instrumentation and working on a variety of sample materials. The analytical precision of the data obtained may be readily determined by a laboratory, but the accuracy and transferability of results remain largely untested. There is a need for a suite of reference samples of known maturity, so that laboratories can perform in-house calibrations with a sub-sample set and then test the accuracy and precision of the calibration curve on another sub-sample set (Lünsdorf et al., 2017). This will make the comparison of vitrinite reflectance and temperature values more reliable between laboratories and allow to better assess and quantify the bias associated with different experimental set-ups, sample preparation and operator bias. Lünsdorf et al. (2017) have pioneered this work and compiled a set of 25 reference samples from the central and western Alps that covers the temperature range of c.160–600 °C, which are available upon request from the first author.

Vitrinite reflectance calibration is performed by analysing the reflectance of standards composed of crystalline material such as spinel (0.4%) and yttrium-aluminium-garnet (YAG, 0.9%). However, it is still unclear what the best sample type might be for the calibration of Raman spectrometry; whether it should be OM that has been naturally heated, or OM that has been artificially heated in the laboratory. The latter may exhibit similar Raman parameters to samples that have been matured naturally (Kelemen and Fang, 2001; Zhou et al., 2014; Bonoldi et al., 2016). However, Hackley and Lünsdorf (2018) and Khatibi et al. (2019) demonstrated that Raman parameters derived from artificially heated OM do not follow the same trend as naturally matured samples. Hackley and Lünsdorf (2018) showed that the G_STA and RBS Raman parameters have higher values and the D/G values are lower for artificially heated samples, demonstrating that the artificial samples do not follow the same maturation pathway as natural samples.

In laboratory experiments by Huang et al. (2010), it was shown that under extremely high pressure (1000–6500 MPa), the D1-band red-shifts more than the G-band, decreasing the RBS, and the G-FWHM visually decreases with increasing pressures, suggesting that pressure is retarding the maturity values derived from these Raman parameters. However, it must be noted that the pressures used in this study far exceed pressures for sedimentary rocks and are only applicable to ultra-high-pressure metamorphism. Du et al. (2014) also showed that different pyrolysis set-ups impact the Raman parameters, suggesting that different environmental conditions can yield variable Raman results.

These results demonstrate that: (1) calibration curves constructed using artificially heated samples should be used with caution; (2) different pressures, heating rates and heating length impact the Raman spectrum of OM. It is therefore encouraged that further work on artificially heated samples with varying deformation styles, pressures and heating rates should be performed, and the results compared to samples that have been matured naturally. It must also be acknowledged that calibration curves constructed using naturally matured samples may only be relevant to that geological area.

6. Future

To progress Raman spectroscopy as a geothermometer we need to develop and follow a standardized method and undertake interlaboratory comparison tests, like those performed previously for VR (Hackley et al., 2015). It is recommended that a diverse set of natural reference samples should be assembled and tested. We advise that artificially heated samples should not be used to create calibration curves for diagenesis to metamorphism studies. However, we would encourage experiments to test the effects of different heating rates, pressures and deformation styles, to get a better appreciation of how different environments may impact the Raman spectrum. This will be of particular value for the application of Raman analysis of OM to the interpretation of processes occurring in fault zones.

Suitable reference samples should be: homogenous, with large quantities of material available in order to create sub-sets for several laboratories; fully characterised using a range of maturity proxies, including VR and Rock-Eval™ pyrolysis for diagenesis to metagenesis, and include mineral assemblage and mineral chemistry data for metamorphic studies. An interlaboratory test can then be devised. We recommended that a workflow similar to that illustrated in Fig. 10 should
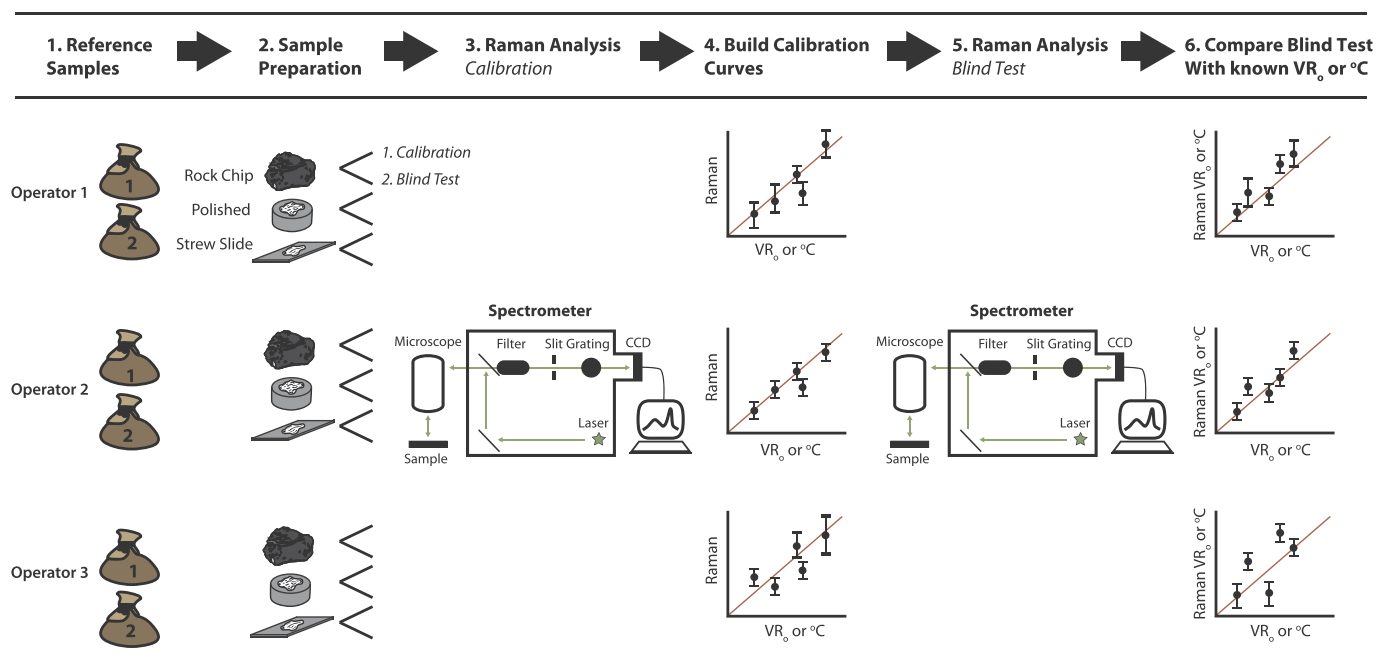
Fig. 10. Example of a future inter-laboratory comparison exercise to determine the bias associated with different methods and different Raman set-ups.

be followed, in order to compare and quantify the bias associated with different instrumental set-ups, sample preparation and operators.

Selected laboratories should receive two suites of reference samples. One sample set will be used for Raman calibration and the other to perform a blind test to assess the accuracy of the calibration curves. Each calibration and blind test sample will be split into three sub-samples that will undergo different sample preparations (polished sections, strew slides and rock chips). Calibration curves will be constructed for each sample type and a blind test performed on each of these. The blind test Raman equivalent VR and temperature values will be compared with the prior measured VR and temperatures values. The results will then be reviewed, and data obtained by different laboratories, sample preparations, Raman instrumentation, and operators will be analysed statistically to identify the elements most subject to bias, and to determine the precision and accuracy of the results obtained using different methodologies.

The deployment of portable Raman instrumentation is also of future interest, as it has the potential to allow operators to perform near real-time maturity analysis on a drilling rig or out in the field when performing metamorphic and structural geology studies. However, this approach has yet to be assessed and the technical feasibility operating in an environment with constant vibration, such as a drilling rig, is debatable. For field analysis, it will be necessary to attach a microscope with either a live streaming camera or eyepiece, so that the operator can target OM particles. Future studies will also need to assess the portable Raman suitability for the analysis of coal and rocks that contain dispersed OM. For dispersed OM, it will be necessary to design a portable Raman instrument with a small laser spot size, similar to the bench-top Raman (c. 2 μm). Having a means to target the OM and have a small laser spot size will help the operator avoid analysing adjacent non-organic grains that can cause fluorescence and obscure the OM Raman bands.

7. Conclusion

Raman spectroscopy offers a cheap, rapid, non-destructive and high-resolution alternative maturity tool than can be used independently or in combination with more conventional methods in order to: (1) reduce the risk in determining the maturity of source rocks during hydrocarbon exploration; (2) determine temperatures associated with contact and/or regional metamorphism; (3) quantify the amount of frictional heating and deformation that has occurred along fault zones.

The G-FWHM and RBS parameters are the most reliable Raman variables that can be used to estimate the maturity of OM during diagenesis–metagenesis, whereas multiple parameters, including the R1, R2, RA1, RA2 and D1-FWHM, have proved to be robust for quantifying the temperatures reached by organic matter in metamorphic rocks. Using integrated areas from the whole spectrum to derive Raman parameters like SSA, D_STA and G_STA is also promising, as these have a wide temperature range. Raman studies of organic matter in fault zones are still in their infancy, but they have great potential to determine not only maximum temperatures attained during frictional heating, but also to shed light on deformation processes.

To promote the wider application of Raman spectroscopy, the terminology for the Raman bands, and the definition and derivation of Raman parameters must be standardized. A unified terminology is proposed here and this should be universally adopted in the future. Raman reference materials are needed, so that inter-laboratory tests can be performed to better determine which methodology, Raman parameters and Raman instrumental set-ups introduce the least bias and generate the most precise and accurate maturity data.

References

Allen, P.A., Allen, J.R., 2013. Basin Analysis: Principles and Application to Petroleum Play Assessment, Third edn. Wiley-Blackwell, Oxford (619pp).

Allwood, C.A., Walter, M.R., Marshall, C.P., 2006. Raman spectroscopy reveals thermal palaeoenvironments of c.3.5 billion-year-old organic matter. Vib. Spectrosc. 41, 190–197.

Ammar, M.R., Rouzaud, J.N., 2012. How to obtain a reliable structural characterization of polished graphitized carbons by Raman microspectroscopy. J. Raman Spectrosc. 41, 207–211.

Aoya, M., Kouketsu, Y., Endo, S., Shimizu, H., Mizukami, T., Nakamura, D., Wallis, S.,

2010. Extending the applicability of the Raman carbonaceous material geothermometer using data from contact metamorphic rocks. J. Metamorph. Geol. 28, 895–914.

Baludikay, B., François, C., Sforna, M., Beghin, J., Cornet, Y., Storme, J., Fagel, N., Fontaine, F., Littke, R., Baudet, D., Delvaux, D., Javaux, E., 2018. Raman microspectroscopy, bitumen reflectance and illite crystallinity scale: comparison of different geothermometry methods on fossiliferous Proterozoic sedimentary basins (DR Congo, Mauritania and Australia). Int. J. Coal Geol. 191, 80–94.

Barzoi, S.C., 2015. Shear stress in the graphitization of carbonaceous matter during the low-grade metamorphism from the northern Parang Mountains (South Carpathians) - Implications to graphite geothermometry. Int. J. Coal Geol. 146, 179–187.

Beny-Bassez, C., Rouzaud, J.N., 1985. Characterization of carbonaceous materials by correlated electron and optical microscopy and Raman microspectroscopy. Scan. Electron Microsc. 1, 119–132.

Bernard, S., Benzerara, K., Beyssac, O., Balan, E., Brown, G.E., 2015. Evolution of the macromolecular structure of sporopollenin during thermal degradation. Heliyon 1 (1–28).

Beyssac, O., Goffé, B., Chopin, C., Rouzaud, J.N., 2002. Raman spectra of carbonaceous material in metasediments: a new geothermometer. J. Metamorph. Geol. 20, 859–871.

Beyssac, O., Goffé, B., Petitet, J.-P., Froigneux, E., Moreau, M., Rouzaud, J.-N., 2003. On the characterization of disordered and heterogenous carbonaceous materials by Raman spectroscopy. Spectrochim. Acta 59, 2267–2276.

Beyssac, O., Pattison, D.R.M., Bourdelle, F., 2019. Contrasting degrees of recrystallization of carbonaceous material in the Nelson aureole, British Columbia and Ballachulish aureole, Scotland, with implications for thermometry based on Raman spectroscopy of carbonaceous material. J. Metamorph. Geol. 37, 71–95.

Bonal, L., Bourot-Denise, M., Quirico, E., Montagnac, G., Lewin, E., 2007. Organic matter and metamorphic history of CO chondrites. Geochim. Cosmochim. Acta 71, 1605–1623.

Bonoldi, L., Di Paolo, L., Flego, C., 2016. Vibrational spectroscopy assessment of kerogen maturity in organic-rich source rocks. Vib. Spectrosc. 87, 14–19.

Brolly, C., Parnell, J., Bowden, S., 2016. Raman spectroscopy: caution when interpreting organic carbon from oxidising environments. Planet. Space Sci. 121, 53–59.

Buseck, P.R., Beyssac, O., 2014. From organic matter to graphite: Graphitization. Elements 10, 421–426.

Cao, S., Neubauer, F., 2019. Graphitic material in fault zones: Implications for fault strength and carbon cycle. Earth-Sci. Rev. 194, 109–124.

Carr, A.D., 2000. Suppression and retardation of vitrinite reflectance, part 1. Formation and significance for hydrocarbon generation. J. Pet. Geol. 23, 313–343.

Chen, Z., Liu, J., Elsworth, D., Connell, L., Pan, Z., 2009. Investigation of CO_2 injection induced coal-gas interactions. In: 43rd U.S. Rock Mechanics Sympo. Asheville, NC.

Chen, S., Wu, D., Liu, G., Sun, R., 2017. Raman spectral characteristics of magmatic-contact metamorphic coals from Huainan Coalfield, China. Spectrochim. Acta A: Molec. Biomolec. Spectrosc. 171, 31–39.

Chesire, S., Craddock, P.R., Xu, G., Sauerer, B., Pomerantz, A.E., McCormick, D., Abdallah, W., 2017. Assessing thermal matuirity beyond the reaches of vitrinite reflectance and Rock-Eval pyrolysis: a case study from the Silurian Qusaiba formation. Int. J. Coal Geol. 180, 29–45.

Childress, L.B., Jacobsen, S.D., 2017. High-pressure high-temperature Raman spectroscopy of kerogen: Relevance to subducted organic carbon. Am. Mineral. 102, 391–403.

Chim, L.K., Yen, J.-Y., Huang, S.-Y., Liou, Y.-S., Tsai, L.L.-Y., 2018. Using Raman spectroscopy of carbonaceous materials to track exhumation of an orogenic belt: an example from Eastern Taiwan. J. Asian Earth Sci. 164, 248–259.

Court, R.W., Sephton, M.A., Parnell, J., Gilmour, I., 2007. Raman spectroscopy of irradiated organic matter. Geochim. Cosmochim. Acta 71, 2547–2568.

Cuesta, A., Dhamelincourt, P., Laureyns, J., 1994. Raman microprobe studies on carbon materials. Carbon 32, 1523–1532.

Delarue, F., Rouzaud, J.-N., Derenne, S., Bourbin, M., Westall, F., Kremer, B., Sugitani, K., Deldicque, D., Robert, F., 2016. The Raman-derived carbonization continuum: a tool to select the best-preserved molecular structures in Archean kerogens. Astrobiology 16, 407–417.

Delchini, S., Lahfid, A., Plunder, A., Michard, A., 2016. Applicability of the RSCM geothermometry approach in a complex tectono-metamorphic context: the Jebilet massif case study (Variscan Belt, Morocco). Lithos 256–257, 1–12.

Du, J., Geng, A., Liao, Z., Cheng, B., 2014. Potential Raman parameters to assess the thermal evolution of kerogens from different pyrolysis experiments. J. Anal. Appl. Pyrolysis 107, 242–249.

Eichmann, S.L., Jacobi, D., Haque, M.H., Burnham, N.A., 2018. Non-destructive investigation of the thermal maturity and mechanical properties of source rocks. J. Pet. Geol. 41, 421–446.

Endo, S., Wallis, R., Tsuboi, M., Torres de Leon, R., Solari, L.A., 2012. Metamorphic evolution of lawsonite eclogites from the southern Motagua fault zone, Guatemala: Insights from phase equilibria and Raman spectroscopy. J. Metamorph. Geol. 30, 143–164.

Ferralis, N., Matys, E.D., Knoll, A.H., Hallmann, C., Summons, R.E., 2016. Rapid, direct and non-destructive assessment of fossil organic matter via micro-Raman spectroscopy. Carbon 108, 440–449.

Ferrari, A.C., Robertson, J., 2001. Resonant Raman spectroscopy of disordered, amorphous, and diamondlike carbon. Phys. Rev. B 64, 075414.

Fomina, E., Kozlov, E., Lokhov, K., Lokhova, O., Bocharov, V., 2019. Carbon sources and the graphitization of carbonaceous matter in Precambrian rocks of the Keivy Terrane (Kola Peninsula, Russia). Minerals 9, 94.

Furuichi, H., Ujiie, K., Kouketsu, Y., Saito, T., Tsutsumi, A., Wallis, S., 2015. Vitrinite reflectance and Raman spectra of carbonaceous material as indicators of frictional heating on faults: Constraints from friction experiments. Earth Planet. Sci. Lett. 424, 191–200.

Golubev, Y.A., Martirosyan, O.V., Kuzmin, D.V., Isaenko, S.I., Makeev, B.A., Antonets, I.V., Utkin, A.A., 2019. Transformations of natural bitumens of different degrees of metamorphism at a low vacuum heating in the temperature range of 400–1000 ℃. J. Pet. Sci. Eng. 173, 315–325.

Goryl, M., Banasik, K., Smolarek-Lach, J., Marynowski, L., 2019. Utility of Raman spectroscopy in estimates of the thermal maturity of Ediacaran organic matter: an example from the east European Craton. Geochemistry https://doi.org/10.1016/j.chemer.2019.06.001. in press.

Guedes, A., Noronha, F., Prieto, A.C., 2005. Characterisation of dispersed organic matter from lower Palaeozoic metasedimentary rocks by organic petrography, X-ray diffraction and micro-Raman spectroscopy analyses. Int. J. Coal Geol. 62, 237–249.

Guedes, A., Valentim, B., Prieto, A.C., Rodrigues, S., Noronha, F., 2010. Micro-Raman spectroscopy of collotelinite, fusinite and macrinite. Int. J. Coal Geol. 83, 415–422.

Guedes, A., Valentim, B., Prieto, A.C., Noronha, F., 2012. Raman spectroscopy of coal macerals and fluidized bed char morphotypes. Fuel 97, 443–449.

Hackley, P.C., Cardott, B.J., 2016. Application of organic petrography in North American shale petroleum systems: a review. Int. J. Coal Geol. 163, 8–51.

Hackley, P.C., Lünsdorf, N.K., 2018. Application of Raman spectroscopy as thermal maturity probe in shale petroleum systems: Insights from natural and artificial maturation series. Energy Fuel 32, 11190–11202.

Hackley, P.C., Araujo, C.V., Borrego, A.G., Bouzinos, A., Cardott, B., Cook, A.C., Eble, C., Flores, D., Gentzis, T., Gonçalves, P.A., Mendonça-Filho, J.G., Hámor-Vidó, M., Jelonek, I., Kommeren, K., Knowles, W., Kus, J., Mastalerz, M., Menezes, T.R., Newman, J., Oikonomopoulos, I.K., Pawlewicz, M., Pickel, W., Potter, J., Ranasinghe, P., Read, H., Reyes, J., Rodriguez, G.D.L.R., Fernandes de Souza, I.V.A., Suarez-Ruiz, I., Sýkorová, I., Valentine, B.J., 2015. Standardization of reflectance measurements in dispersed organic matter: results of an exercise to improve interlaboratory agreement. Mar. Pet. Geol. 59, 22–34.

Hara, H., Hara, K., 2018. Radiolarian and U–Pb zircon dating of Late Cretaceous and Paleogene Shimanto accretionary complexes, Southwest Japan: Temporal variations in provenance and offset across an out-of-sequence thrust. J. Asian Earth Sci. 170, 29–44.

Hara, H., Kurihara, T., Mori, H., 2013. Tectono-stratigraphy and low-grade metamorphism of Late Permian and Early Jurassic accretionary complexes within the Kurosegawa belt, Southwest Japan: Implications for mechanisms of crustal displacement within active continental margin. Tectonophysics 592, 80–93.

Hartkopf-Fröder, C., Königshof, P., Littke, R., Schwarzbauer, J., 2015. Optical thermal maturity parameters and organic geochemical alteration at low grade diagenesis to anchimetamorphism: a review. Int. J. Coal Geol. 150–151, 74–119.

Henry, D.G., Jarvis, I., Gillmore, G., Stephenson, M., Emmings, J., 2018. Assessing low-maturity organic matter in shales using Raman spectroscopy: Effects of sample preparation and operating procedure. Int. J. Coal Geol. 191, 135–151.

Henry, D.G., Jarvis, I., Gillmore, G., Stephenson, M., 2019. A rapid method for determining organic matter maturity using Raman spectroscopy: Application to Carboniferous organic-rich mudstones and coals. Int. J. Coal Geol. 203, 87–98.

Hinrichs, R., Brown, M.T., Vasconcellos, M.A.Z., Abrashev, M.V., Kalkreuth, W., 2014. Simple procedure for an estimation of the coal rank using micro-Raman spectroscopy. Int. J. Coal Geol. 136, 52–58.

Hirono, T., Maekawa, Y., Yabuta, H., 2015. Investigation of the records of earthquake slip in carbonaceous materials from the Taiwan Chelungpu fault by means of infrared and Raman spectroscopies. Geochem. Geophys. Geosyst. 16, 1233–1253.

Hoinkes, G., Hauzenberger, C.A., Schmid, R., 2005. Metamorphic rocks: Classification, nomenclature, and formation. In: Selley, R., Cocks, R., Plimer, I. (Eds.), Encyclopedia of Geology, pp. 386–402.

Hou, Y., Zhang, K., Wang, F., He, S., Dong, T., Wang, C., Qin, W., Xiao, Y., Tang, B., Yu, R., Du, X., 2019. Structural evolution of organic matter and implications for graphitization in overmature marine shales, South China. Mar. Pet. Geol. 109, 304–316.

Hu, S., Evans, K., Craw, D., Rempel, K., Bourdet, J., Dick, J., Grice, K., 2015. Raman characterization of carbonaceous material in the Macraes orogenic gold deposit and metasedimentary host rocks, New Zealand. Ore Geol. Rev. 70, 80–95.

Huan, X., Tang, Y.-G., Xu, J.-J., Lan, C.-Y., Wang, S.-Q., 2019. Structural characterization of graphenic material prepared from anthracites of different characteristics: A comparative analysis. Fuel Process. Technol. 183, 8–18. https://doi.org/10.1016/j.fuproc.2018.08.017.

Huang, E.P., Huang, E., Yu, S.-C., Chen, Y.-H., Lee, J.-S., Fang, J.-N., 2010. In situ Raman spectroscopy on kerogen at high temperatures and high pressures. Phys. Chem. Miner. 37, 593–600.

Inan, S., Goodarzi, F., Mumm, A.S., Arouri, K., Qathami, S., Ardakani, O.H., Inan, T., Tuwailib, A.A., 2016. The Silurian Qusaiba Hot Shales of Saudi Arabia: an integrated assessment of the thermal maturity. Int. J. Coal Geol. 159, 107–119.

Ito, K., Ujiie, K., Kagi, H., 2017. Detection of increased heating and estimation of co-seismic shear stress from Raman spectra of carbonaceous material in pseudotachylytes. Geophys. Res. Lett. 44, 1749–1757.

Jarvie, D.M., Claxton, B.L., Henk, F., Breyer, J.T., 2001. Oil and shale gas from the Barnett Shale, Fort Worth basin, Texas. AAPG Annu. Meet. Progr. 10, A100.

Jehlička, J., Beny, C., 1999. First and second order Raman spectra of natural highly carbonified organic compounds from metamorphic rocks. J. Mol. Struct. 480–481, 541–545.

Jehlička, J., Urban, O., Pokorný, J., 2003. Raman spectroscopy of carbon and solid bitumens in sedimentary and metamorphic rocks. Spectrochim. Acta A Mol. Biomolec. Spectrosc. 59, 2341–2352.

Jubb, A.M., Botterell, P.J., Birdwell, J.E., Burruss, R.C., Hackley, P.C., Valentine, D.J., Hatcherian, J.J., Wilson, S.A., 2018. High microscale variability in Raman thermal maturity estimates from shale organic matter. Int. J. Coal Geol. 199, 1–9.

Jurdik, K., Rantitsch, G., Rainer, T.M., Árkai, P., Tomljenovic, B., 2008. Alpine metamorphism of organic matter in metasedimentary rocks from Mt. Medvednica (Croatia). Swiss J. Geosci. 101, 605–616.

Kaneki, S., Hirono, T., 2018. Kinetic effect of heating rate on the thermal maturity of carbonaceous material as an indicator of frictional heat during earthquakes. Earth Planet. Space 70, 92. https://doi.org/10.1186/s40623-018-0868-7.

Kaneki, S., Hirono, T., 2019. Diagenetic and shear-induced transitions of frictional strength of carbon-bearing faults and their implications for earthquake rupture dynamics in subduction zones. Sci. Rep. 9, 7884.

Kaneki, S., Hirono, T., Mukoyoshi, H., Sampei, Y., Ikehara, M., 2016. Organochemical characteristics of carbonaceous materials as indicators of heat recorded on an ancient plate-subduction fault. Geochem. Geosyst. 17, 2855–2868.

Kaneki, S., Ichiba, T., Hirono, R., 2018. Mechanochemical effect on maturation of carbonaceous material: Implications for thermal maturity as a proxy for temperature in estimation of coseismic slip parameters. Geophys. Res. Lett. 45, 2248–2256.

Kelemen, S.R., Fang, H.L., 2001. Maturity trends in Raman spectra from kerogen and coal. Energy Fuel 15, 653–658.

Khatibi, S., Ostadhassan, M., Tuschel, D., Gentzis, T., Bubach, B., Carvajal-Ortiz, H., 2018a. Raman spectroscopy to study thermal maturity and elastic modulus of kerogen. Int. J. Coal Geol. 185, 103–118.

Khatibi, S., Ostadhassan, M., Tuschel, D., Gentzis, T., Carvajal-Ortiz, H., 2018b. Evaluating molecular evolution of kerogen by Raman spectroscopy: Correlation with optical microscopy and Rock-Eval pyrolysis. Energies 11, 1406.

Khatibi, S., Ostadhassan, M., Aghajanpour, A., 2018c. Raman spectroscopy: an analytical tool for evaluating organic matter. J. Oil Gas Petrochem. Sci. 1, 28–33.

Khatibi, S., Ostadhassan, M., Hackley, P., Tuschel, D., Abarghani, A., Bubach, B., 2019. Understanding organic matter heterogeneity and maturation rate by Raman spectroscopy. Int. J. Coal Geol. 206, 46–64.

Kirilova, M., Toy, V., Rooney, J.S., Giorgetti, C., Gordon, K.C., Collettini, C., Takeshita, T., 2018. Structural disorder of graphite and implications for graphite thermometry. Solid Earth 9, 223–231.

Kitamura, M., Mukoyoshi, H., Fulton, P.M., Hirose, T., 2012. Coal maturation by frictional heat during rapid fault slip. Geophys. Res. Lett. 39, 1–5.

Kouketsu, Y., Mizukami, T., Mori, H., Endo, S., Aoya, M., Hara, H., Nakamura, D., Wallis, S., 2014. A new approach to develop the Raman carbonaceous material geothermometer for low grade metamorphism using peak width. Island Arc 23, 33–50.

Kouketsu, Y., Shimizu, I., Wang, Y., Yao, L., Ma, S., Shimamoto, T., 2017. Raman spectra of carbonaceous materials in a fault zone in the Longmenshan thrust belt, China: Comparisons with those of sedimentary and metamorphic rocks. Tectonophysics 699, 129–145.

Kouketsu, Y., Tsai, C.H., Enami, M., 2019a. Discovery of unusual metamorphic temperatures in the Yuli belt, eastern Taiwan: New interpretation of data by Raman carbonaceous material geothermometry. Geology 47, 522–526.

Kouketsu, Y., Miyake, A., Igami, Y., Taguchi, T., Kagi, H., Enami, M., 2019b. Drastic effect of shearing on graphite microtexture: attention and application to Earth science. Prog. Earth Planet. Sci. 6, 23. https://doi.org/10.1186/s40645-019-0271-4.

Kribek, B., Hrabal, J., Landais, P., Hladíkova, J., 1994. The association of poorly ordered graphite, coke and bitumnes in greenschist facies rocks of the Poniklá Group, Lugicum, Czech Republic: the results of graphitization of various types of carbonaceous matter. J. Metamorph. Geol. 12, 493–503.

Kuo, L.W., Felice, F.D., Spagnuolo, E., Di Toro, G., Song, S.R., Aretusini, S., Li, H., Suppe, J., Si, J., Wen, C.Y., 2017. Fault gouge graphitization as evidence of past seismic slip. Geology 45, 979–982.

Kuo, L.W., Huang, J.R., Fang, J.N., Si, J., Li, H., Song, S.R., 2018. Carbonaceous materials in the fault zone of the Longmenshan Falt Belt: 1. Signatures within the deep Wenchuan earthquake fault zone and their implications. Minerals 8, 385.

Lahfid, A., Beyssac, O., Deville, E., Negro, F., Chopin, C., Goffé, B., 2010. Evolution of the Raman spectrum of carbonaceous material in low-grade metasediments of the Glarus Alps (Switzerland). Terra Nova 22, 354–360.

Landis, C.A., 1971. Graphitisation of dispersed carbonaceous material in metamorphic rocks. Contrib. Mineral. Petrol. 30, 34–45.

Lespade, P., Al-Jishi, R., Dresselhaus, M.S., 1982. Model for Raman scattering from incompletely graphitized carbons. Carbon 20, 427–431.

Li, C.-Z., 2007. Some recent advances in the understanding of the pyrolysis and gasification behaviour of Victorian brown coal. Fuel 86, 1664–1683.

Li, X., Hayashi, J.-I., Li, C.-Z., 2006. FT-Raman spectroscopic study of the evolution of char structure during the pyrolysis of a Victorian brown coal. Fuel 85, 1700–1707.

Liu, D., Xiao, X., Tian, H., Min, Y., Zhou, Q., Cheng, P., Shen, J., 2013. Sample maturation calculated using Raman spectroscopic parameters for solid organics: Methodology and geological applications. Chin. Sci. Bull. 58, 1285–1298.

Liu, J., Li, H., Zhang, J., Zhang, B., 2016. Origin and formation of carbonaceous material veins in the 2008 Wenchuan earthquake fault zone. Earth Planet. Space 68, 19.

Lünsdorf, N.K., 2016. Raman spectroscopy of dispersed vitrinite - Methodical aspects and correlation with reflectance. Int. J. Coal Geol. 153, 75–86.

Lünsdorf, N.K., Lünsdorf, J.O., 2016. Evaluating Raman spectra of carbonaceous matter by automated, iterative curve-fitting. Int. J. Coal Geol. 160–161, 51–62.

Lünsdorf, N.K., Dunkl, I., Schmidt, B.C., Rantitsch, G., von Eynatten, H., 2014. Towards a higher comparability of geothermometric data obtained by Raman spectroscopy of carbonaceous material. Part I: Evaluation of biasing factors. Geostand. Geoanal. Res. 38, 73–94.

Lünsdorf, N.K., Dunkl, I., Schmidt, B.C., Rantitsch, G., von Eynatten, H., 2017. Towards a higher comparability of geothermometric data obtained by Raman spectroscopy of carbonaceous material. Part 2: a revised geothermometer. Geostand. Geoanal. Res. 41, 593–612.

Lupoi, J.S., Fritz, L.P., Parris, T.M., Hackley, P.C., Solotky, L., Eble, C.F., Schlaegle, S., 2017. Assessment of thermal maturity trends in Devonian–Mississippian source rocks

using Raman spectroscopy: Limitations of peak-fitting method. Front. Energy Res. 5, 24.

Lupoi, J.S., Fritz, L.P., Hackley, P.C., Solotky, L., Weislogel, A., Schlaegle, S., 2018. Quantitative evaluation of vitrinite reflectance and atomic O/C in coal using Raman spectroscopy and multivariate analysis. Fuel 230, 1–8.

Lupoi, J.S., Hackley, P.C., Birsic, E., Fritz, L.P., Solotky, L., Weislogel, A., Schlaegle, S., 2019. Quantitative evaluation of vitrinite reflectance in shale using Raman spectroscopy and multivariate analysis. Fuel 254, 115573. https://doi.org/10.1016/j.fuel. 2019.05.156.

Marques, M., Suárez-Ruiz, I., Flores, D., Guede, A., Rodrigues, S., 2009. Correlation between optical, chemical and micro-structural parameters of high-rank coals and graphite. Int. J. Coal Geol. 77, 377–382.

Marshall, C., Javaux, E., Knoll, A., Walter, M., 2005. Combined micro-Fourier transform infrared (FTIR) spectroscopy and micro-Raman spectroscopy of Proterozoic acritarchs: a new approach to palaeobiology. Precambrian Res. 138, 208–224.

Mathew, G., De Sarker, S., Pande, K., Dutta, S., Ali, S., Rai, A., Netrawali, S., 2013. Thermal metamorphism of the Arunachal Himalaya, India: Raman thermometry and thermochronological constraints on the tectono-thermal evolution. Int. J. Earth Sci. 102, 1911–1936.

McNeil, D.H., Schulze, H.G., Matys, E., Bosak, T., 2016. Raman spectroscopic analysis of carbonaceous matter and silica in the test walls of recent and fossil agglutinated foraminifera. AAPG Bull. 99, 1081–1097.

Mészáros, E., Varga, A., Raucsik, B., Benkó, Z., Heincz, A., Hauzenberger, C.A., 2019. Provenance and Variscan low-grade regional metamorphism recorded in slates from the basement of the (SW Hungary). Int. J. Earth Sci. 1–23.

Mi, J., He, K., Fan, J., Hu, G., Zhang, B., 2019. Thermal maturity determination for oil prone organic matter based on the Raman spectra of artificial matured samples. Vib. Spectrosc. 102940. in press. https://doi.org/10.1016/j.vibspec.2019.102940.

Mori, H., Mori, N., Wallis, S., Westaway, R., Annen, C., 2017. The importance of heating duration for Raman CM thermometry: evidence from contact metamorphism around the Great Whin Sill intrusion, UK. J. Metamorph. Geol. 35, 165–180.

Muirhead, D.K., Parnell, J., Spinks, S., Bowden, S.A., 2017a. Characterization of organic matter in the Torridonian using Raman spectroscopy. In: Brasier, A.T., Mcilroy, D., Mcloughlin, N. (Eds.), Earth System Evolution and Early Life: A Celebration of the Work of Martin Brasier. 448. Geol. Soc. London Spec. Publ, pp. 71–80.

Muirhead, D.K., Bowden, S.A., Parnell, J., Schofield, N., 2017b. Source rock maturation due to igneous intrusion in rifted margin petroleum systems. J. Geol. Soc. Lond. 174, 979.

Mukoyoshi, H., Kaneki, S., Hirono, T., 2018. Slip parameters on major thrusts at a convergent plate boundary: Regional heterogeneity of potential slip distance at the shallow portion of the subducting plate. Earth Planet. Space 70, 36.

Mumm, A.S., Inan, S., 2016. Microscale organic maturity determination of graptolites using Raman spectroscopy. Int. J. Coal Geol. 162, 96–107.

Nakamura, Y., Oohashi, K., Toyoshima, T., Satish-Kumar, M., Akai, J., 2015. Strain-induced amorphization of graphite in fault zones of the Hidaka metamorphic belt, Hokkaido, Japan. J. Struct. Geol. 72, 142–161.

Nakamura, Y., Yoshino, T., Satish-Kumar, M., 2017. An experimental kinetic study on the structural evolution of natural carbonaceous material to graphite. Am. Mineral. 102, 135–148.

Nakamura, Y., Hara, H., Kagi, H., 2019. Natural and experimental structural evolution of dispersed organic matter in mudstones: the Shimano accretionary complex, Southwest Japan. Island Arc E12318. https://doi.org/10.1111/iar.12318.

Nestler, K., Dietrich, D., Witke, K., Rößler, R., Marx, G., 2003. Thermogravimetric and Raman spectroscopic investigations on different coals in comparison to dispersed anthracite found in permineralized tree fern *Psaronius* sp. J. Mol. Struct. 661–662, 357–362.

Oohashi, K., Hirose, T., Shimamoto, T., 2011. Shear-induced graphitization of carbonaceous materials during seismic fault motion: experiments and possible implications for fault mechanics. J. Struct. Geol. 33, 1122–1134.

Pan, J., Lv, M., Hou, Q., Han, Y., Wang, K., 2019. Coal microcrystalline structural changes related to methane adsorption/desorption. Fuel 239, 13–23.

Pasteris, J.D., 1989. In situ analysis in geological thin-sections by laser Raman microprobe microscopy: a cautionary note. Appl. Spectrosc. 43, 567–570.

Pasteris, J.D., Wopenka, B., 1991. Raman spectra of graphite as indicators of degree of metamorphism. Can. Mineral. 29, 1–9.

Pawlyta, M., Rouzaud, J.N., Duber, S., 2015. Raman microspectroscopy characterization of carbon blacks: Spectral analysis and structural information. Carbon 84, 479–490.

Quirico, E., Rouzaud, J., Bonal, L., Montagnac, G., 2005. Maturation grade of coals as revealed by Raman spectroscopy: Progress and problems. Spectrochim. Acta A Mol. Biomol. Spectrosc. 61, 2368–2377.

Quirico, E., Bourot-denise, M., Robin, C., Montagnac, G., Beck, P., 2011. A reappraisal of the metamorphic history of EH3 and EL3 enstatite chondrites. Geochim. Cosmochim. Acta 75, 3088–3102.

Rahl, J.M., Anderson, K.M., Brandon, M., Fassoulas, C., 2005. Raman spectroscopic carbonaceous material thermometry of low-grade metamorphic rocks: Calibration and application to tectonic exhumation in Crete, Greece. Earth Planet. Sci. Lett. 240, 339–354.

Rantitsch, G., Grogger, W., Teichert, C., Ebner, F., Hofer, C., Maurer, E.M., Schaffer, B., Toth, M., 2004. Conversion of carbonaceous material to graphite within the Greywacke Zone of the Eastern Alps. Int. J. Earth Sci. 93, 959–973.

Rantitsch, G., Lämmerer, W., Fisslthaler, E., Mitsche, S., Kaltenböck, H., 2016. On the discrimination of semi-graphite and graphite by Raman spectroscopy. Int. J. Coal Geol. 159, 49–56.

Rantitsch, G., Bhattacharyya, A., Schenk, J., 2019. Microstructural evolution of blast furnace coke during experimental heating – the IFORS approach. Berg–Huettenmaenn. Monatsh. 164, 257–260.

Roberts, S., Tricker, P.M., Marshall, J.E.A., 1995. Raman spectroscopy of chitinozoans as a maturation indicator. Org. Geochem. 23, 223–228.

Romero-Sarmiento, M.F., Rouzaud, J.N., Bernard, S., Deldicque, D., Thomas, M., Littke, R., 2014. Evolution of Barnett Shale organic carbon structure and nanostructure with increasing maturation. Org. Geochem. 71, 7–16.

Sauerer, B., Craddock, P.R., Aljohani, M.D., Alsamadony, K.L., Abdallah, W., 2017. Fast and accurate shale maturity determination by Raman spectroscopy measurement with minimal sample preparation. Int. J. Coal Geol. 173, 150–157.

Scharf, A., Handy, M.R., Ziemann, M.A., Schmid, S.M., 2013. Peak-temperature patterns of polyphase metamorphism resulting from accretion, subduction and collision (eastern Tauern window, European alps) – a study with Raman microspectroscopy on carbonaceous material (RSCM). J. Metamorph. Geol. 31, 863–880.

Schiffbauer, J.D., Wallace, A.F., Hunter, J.L.-J., Kowalewski, M., Bodnar, R.J., Xiao, S., 2012. Thermally-induced structural and chemical alteration of organic-walled microfossils: an experimental approach to understanding fossil preservation in metasediments. Geobiol 10, 402–423.

Schito, A., Corrado, S., 2018. An automatic approach for characterization of the thermal maturity of dispersed organic matter Raman spectra at low diagenetic stages. In: Dowey, P., Osborne, M., Volk, H. (Eds.), Application of Analytical Techniques to Petroleum Systems. 484 Geol. Soc. London Spec. Publ. https://doi.org/10.1144/SP484.5.

Schito, A., Romano, C., Corrado, S., Grigo, D., Poe, B., 2017. Diagenetic thermal evolution of organic matter by Raman spectroscopy. Org. Geochem. 106, 57–67.

Schito, A., Spina, A., Corrado, S., Cirilli, S., Romano, C., 2019. Comparing optical and Raman spectroscopic investigations of phytoclasts and sporomorphs for thermal maturity assessment: the case study of Hettangian continental facies in the Holy cross Mts. (central Poland). Mar. Pet. Geol. 104, 331–345.

Schmidt, J.L., Hinrichs, R., Araujo, C.V., 2017. Maturity estimation of phytoclasts in strew mounts by micro-Raman spectroscopy. Int. J. Coal Geol. 173, 1–8.

Schopf, J.W., Kudryavtsev, A.B., Agresti, D.G., Czaja, A.D., Wdowiak, T.J., 2005. Raman imagery: a new approach to assess the geochemical maturity and biogenicity of permineralized Precambrian fossils. Astrobiol 5, 333–371.

Song, Y., Jiang, C., Qu, M., 2019. Macromolecular evolution and structural defects in tectonically deformed coals. Fuel 236, 1432–1445.

Spötl, C., Houseknecht, D.W., Jaques, R.C., 1998. Kerogen maturation and incipient graphitization of hydrocarbon source rocks in the Arkoma Basin, Oklahoma and Arkansas: a combined petrographic and Raman spectrometric study. Org. Geochem. 28, 535–542.

Starkey, N.A., Franchi, I.A., Alexander, C.M.O., 2013. A Raman spectroscopic study of organic matter in interplanetary dust particles and meteorites using multiple wavelength laser excitation. Meteorit. Planet. Sci. 48, 1800–1822.

Tissot, B.P., Welte, D.H., 1984. Petroleum Formation and Occurrence, 2nd Ed. Springer-Verlag, Berlin (699 p).

Tunistra, F., Koenig, J.L., 1970. Raman spectrum of graphite. J. Chem. Phys. 53, 1126.

Ulyanova, E.V., Molchanov, A.N., Prokhorov, I.Y., Grinyov, V.G., 2014. Fine structure of Raman spectra in coals of different rank. Int. J. Coal Geol. 121, 37–43.

Vidano, R.P., Fischbach, D.B., Willis, L.J., Loehr, T.M., 1981. Observation of Raman band shifting with excitation wavelength for carbons and graphites. Solid State Commun. 39, 341–344.

Villanueva, U., Raposo, J.C., Castro, K., de Diego, A., Arana, G., Madariaga, J.M., 2008. Raman spectroscopy speciation of natural and anthropogenic solid phases in river and estuarine sediments with appreciable amount of clay and organic matter. J. Raman Spectrosc. 39, 1195–1203.

Wang, Y., Qiu, N., Borjigin, T., Shen, B., Xie, X., Ma, Z., Lu, C., Yang, Y., Yang, L., Cheng, L., Fang, G., Cui, Y., 2018. Integrated assessment of thermal maturity of the Upper Ordovician–Lower Silurian Wufeng–Longmaxi shale in Sichuan Basin, China. Mar. Pet. Geol. 100, 447–465.

Wilkins, R.W.T., Boudou, R., Sherwood, N., Xiao, X., 2014. Thermal maturity evaluation from inertinites by Raman spectroscopy: the 'RaMM' technique. Int. J. Coal Geol. 128, 143–152.

Wilkins, R.W.T., Wang, M., Gan, H., Li, Z., 2015. A RaMM study of thermal maturity of dispersed organic matter in marine source rocks. Int. J. Coal Geol. 150–151, 252–264.

Wilkins, R.W.T., Sherwood, N., Li, Z., 2018. RaMM (Raman maturity method) study of samples used in an interlaboratory exercise on a standard test method for determination of vitrinite reflectance on dispersed organic matter in rocks. Mar. Pet. Geol. 91, 236–250.

Wopenka, B., Pasteris, J.D., 1993. Structural characterization of kerogens to granulite-facies graphite: Applicability of Raman microprobe spectroscopy. Am. Mineral. 78, 533–577.

Yoshida, A., Kaburagi, Y., Hishiyama, Y., 2006. Full width at half maximum intensity of the G band in the first order Raman spectrum of carbon material as a parameter for graphitization. Carbon 44, 2330–2356.

Yu, W., Polgari, M., Gyollai, I., Fintor, K., Szabo, M., Kovács, I., Fekete, J., Du, Y., Zhou, Q., 2019. Microbial metallogenesis of Cryogenian manganese ore deposits in South China. Precambrian Res. 322, 122–135.

Yuman, W., Xinjing, L., Bo, C., Wei, W., Dazhong, D., Jian, Z., Jing, H., Jie, M., Bing, D., Hao, W., Shan, J., 2018. Lower limit of thermal maturity for the carbonization of organic matter in marine shale and its exploration risk. Pet. Explor. Dev. 45, 402–411.

Zeng, Y., Wu, C., 2007. Raman and infrared spectroscopic study of kerogen treated at elevated temperatures and pressures. Fuel 86, 1192–1200.

Zhang, Y., Li, Z., 2019. Raman spectroscopic study of chemical structure and thermal maturity of vitrinite from a suite of Australia coals. Fuel 241, 188–198.

Zhang, C., Santosh, M., 2019. Coupled laser Raman spectroscopy and carbon stable isotopes of graphite from the khondalite belt of Kerala, southern India. Lithos 334–335, 245–253.

Zhou, Q., Xiao, X., Pan, L., Tian, H., 2014. The relationship between micro-Raman spectral parameters and reflectance of solid bitumen. Int. J. Coal Geol. 121, 19–25.